Forecasting Research

Forecasting Research Division
Scientific Paper No. 35

An evaluation of semi-Lagrangian advection schemes in simulations of rotating, stratified flows in the laboratory

Final report of Contract Met 2a/0541

by

P L Read and N P J Thomas

May 1995

Meteorological Office
London Road
Bracknell
Berkshire
RG12 2SZ
United Kingdom

Forecasting Research Division
Scientific Paper No. 35

An evaluation of semi-Lagrangian advection schemes in simulations of rotating, stratified flows in the laboratory

Final report of Contract Met 2a/0541

by

P L Read and N P J Thomas

May 1995

AN EVALUATION OF SEMI-LAGRANGIAN ADVECTION SCHEMES IN SIMULATIONS OF ROTATING, STRATIFIED FLOWS IN THE LABORATORY

P. L. Read and N. P. J. Thomas

Atmospheric, Oceanic & Planetary Physics, Clarendon Laboratory,
Parks Road, Oxford, OX1 3PU, United Kingdom

Submitted to *Quart. J. R. Met. Soc.* May 1995

ABSTRACT

A series of numerical simulations of steady and time-dependent thermally-stratified flow in a rotating, cylindrical fluid annulus were carried out, including cases of both steady (axisymmetric and 3D waves) and time-dependent (periodically vacillating) flows. A range of different numerical advection schemes were used for the representation of heat transport, including a conventional conservative Eulerian scheme and three different variants of a (fully 3D) semi-Lagrangian scheme. The resulting simulations were compared both with each other, and with high precision measurements of velocity, temperature and total heat transport in the laboratory. In all cases considered, the fully Eulerian simulations gave good quantitative agreement with the laboratory measurements, provided somewhat finer spatial resolution was used than in earlier studies. The performance of the semi-Lagrangian scheme was found to be quite strongly sensitive to the spatial interpolation algorithm. A basic tensor cubic scheme generally produced good simulations of steady 2D and 3D flows, although the somewhat more accurate tensor quintic scheme (which is also more expensive) appeared to offer some detectable improvements in accuracy and performance in some cases. A split cubic scheme (which is computationally cheaper but much less formally accurate) gave generally poor results in practice, and is not recommended. A general problem was encountered, however, with all the semi-Lagrangian schemes in simulating a transition to the highly baroclinic time-dependent amplitude vacillating flow regime, for which all the schemes exhibited an apparent spurious stability. This result suggests a possible generic problem with semi-Lagrangian schemes, which should be considered further before their widespread adoption in operational models.

1. INTRODUCTION

The accurate and efficient representation of advection is a key element in any numerical model of fluid motion, since this gives rise to some of the principal sources of nonlinearity in a fluid system. The requirement to employ schemes which provide the maximum computational efficiency without unduly sacrificing accuracy, stability or conservation properties is of particular concern in the design of models for weather and climate prediction, for which attainment of maximum spatial resolution for a given computational cost is given a high premium.

In the latter context, discretization schemes based on a semi-Lagrangian treatment of advection have received considerable attention during the past 10-15 years, since they offer the prospect of allowing significantly larger timesteps (with no significant loss of formal accuracy) than corresponding Eulerian schemes, whose timestep length is generally limited severely by considerations of stability (see Staniforth & Côté (1991) for a recent review). Such advantages may be further enhanced by the use of a semi-implicit treatment of time-integration (Robert 1981,1982), and this combined approach has been taken up by an increasing range of atmospheric models in recent years. Most applications to date have been in grid-point models, ranging from early three time-level shallow-water models (Robert 1981, 1982; Staniforth & Temperton 1986), two time-level shallow-water schemes (e.g. Temperton & Staniforth 1987; Purser & Leslie 1989; McDonald & Bates 1989; Côté & Staniforth 1990), and various forms of baroclinic primitive equation grid-point model (e.g. three time-level schemes by Robert et al. (1985); Tanguay et al. (1989); and two time-level schemes e.g. by Leslie & Purser (1991); McDonald & Haugen (1992); Bates et al. (1993)). Recent developments have also included applications to non-hydrostatic models (Tanguay et al. (1990); Golding (1992)), and to spectral models (Ritchie (1991); Williams & Olsen (1994); Ritchie et al. (1994)). Of particular interest in the present context is that a similar scheme is currently under consideration for incorporation into the next generation of numerical weather prediction and climate models at the UK Meteorological Office (Cullen et al. 1994).

The essence of the semi-Lagrangian approach to representing advection may be summarised as follows (in a three time-level form for illustration, though the equivalent two time-level scheme is described e.g. by Staniforth & Côté 1991). An advection problem may be written in the general form

$$\frac{DF}{Dt} - G(\mathbf{x}, t) = S(\mathbf{x}, t) \tag{1}$$

where D/Dt is the Lagrangian derivative $(\partial/\partial t + \mathbf{v}.\nabla)$ which follows the motion in a velocity field $\mathbf{v}(\mathbf{x},t)$, $F(\mathbf{x},t)$ is the field being advected and $G(\mathbf{x},t)$ and $S(\mathbf{x},t)$ represent source terms. F is represented on a specified Eulerian grid, fixed in space, and the procedure seeks to compute the appropriate value of F on this grid at a future time $t+\delta t$, given F and $\mathbf{v}$ at times t and $t-\delta t$. Since, apart from source terms G and S, F is conserved following the flow, the trajectory of each point on the grid is integrated backwards in time to its location at $t-\delta t$, termed the departure point $\mathbf{x_d} = \mathbf{x}(t-\delta t)$. The source terms S and G are then interpolated in space either onto the mid-point of the trajectory $\mathbf{x_m}$ or to $\mathbf{x_d}$, F is interpolated onto $\mathbf{x_d}$, and Eq (1) is integrated forwards in time to $t+\delta t$ as

$$F(\mathbf{x},t+\delta t) = F(\mathbf{x_d},t-\delta t) + 2\delta t[(G(\mathbf{x_d},t-\delta t) + G(\mathbf{x},t+\delta t))/2 + S(\mathbf{x_m},t)] \qquad (2)$$

where $\mathbf{x_m}$ is often taken to lie at $(\mathbf{x}+\mathbf{x_d})/2$. Critical elements of the procedure, therefore, typically involve (a) determination of the departure points $\mathbf{x_d}$, and (b) spatial interpolation of the field F and source terms to $\mathbf{x_d}$ and/or $\mathbf{x_m}$, all to sufficient accuracy to preserve the main characteristics of the process.

Various procedures involving differing combinations of iteration and interpolation have been suggested for (a) (e.g. Robert 1981, McGregor 1993), while (b) is generally implemented using cubic or higher order interpolation schemes (linear interpolation is not sufficiently accurate, e.g. see Williamson & Rasch (1989)), though at some significant penalty in computational complexity and cost. An important question is the extent to which compromises may be made, especially in the design of (b), to achieve savings in computer time and storage (since fully 3D tensor forms of cubic and higher order interpolators may entail many operations per grid-point). Some studies, for instance, have suggested the use of split (2 or 3 $\times$ 1D) interpolation as a way of reducing the computational cost (by as much as a factor ~ 3, e.g. see Bates 1984; Golding 1992), though with some sacrifice of formal accuracy. Other uncertainties concern (i) the representation of boundary conditions, especially for limited area models and in the vicinity of orography, and (ii) the role and significance of conservation properties. Semi- Lagrangian schemes do not, in general, possess formal conservation properties which are analogous to those of many Eulerian schemes. While the consequences of non-conservation in semi-Lagrangian advection are generally taken to be modest and largely benign, the absence of such properties is a matter of some concern, especially where such schemes are used for long-term climate studies or for the advection of tracers which interact with parametrization schemes.

The verification and validation of any advection scheme is a further issue of some importance, and forms a key element of the work described herein. Model validation is traditionally carried out by either (a) performing a range of idealized numerical experiments, typically entailing the advection of blobs or patches of a passive tracer across a domain by a known (simple) velocity field, or (b) full implementation of the scheme in question into an operational atmospheric model. In the latter case, the performance of the model is assessed, often somewhat subjectively, by comparison between case study simulations and corresponding atmospheric observations. In the case of (a), gross problems associated e.g. with dispersive phase errors are given clear prominence, usually by choosing tracer distributions with unrealistic and pathological properties such as sharp gradients and corners, though the actual consequences of such errors in practical simulations of dynamical phenomena is often obscure. In the case of (b), although the realism of the problem is guaranteed, the validation is often rendered uncertain because of inadequacies in the observational data and initialisation procedures, and because of uncertainties in the parametrization of unresolved physical processes. For such purposes, the real atmosphere may simply be too complicated and difficult to observe for the performance of conclusive tests.

In the present work, therefore, we make use of a laboratory system to provide the relevant cases to be used for the validation of simulations using a number of semi-Lagrangian advection schemes of current meteorological interest. The flow observed when a cylindrical annulus of liquid is rotated about its axis of symmetry and subject to differential heating at the sidewall boundaries is well known to exhibit a wide variety of flow regimes involving fully- developed manifestations of baroclinic instability (e.g. Hide & Mason 1975). Through careful control of the experimental parameters, flow regimes with differing degrees of spatial and temporal complexity may be obtained, and characterised to high precision in measurements of flow velocity, temperature and heat transfer. Such flow regimes are sufficiently close in behaviour to the large-scale atmosphere to obtain circulations which pose similar dynamical challenges to a numerical model to those obtaining in the atmosphere itself, but without many of the complex and uncertain physical 'forcing processes' which complicate the validation process of atmospheric simulations. The level of experimental control and measurement precision may also be sufficient to enable a conclusive test of a numerical model to be carried out under realistically valid conditions appropriate to a real fluid system (cf James et al. 1981; Hignett et al. 1985 - hereafter referred to as H85).

Section 2 describes the experimental system, while Section 3 outlines the model formulation and the various schemes to be implemented for the advection of temperature. Section 4 introduces the particular flow cases to be used to test the various types of advection schemes. The main results of both 2D axisymmetric and fully 3D semi-Lagrangian simulations are presented in sections 5 and 6.

Some concluding remarks are offered in section 7, together with some recommendations concerning the implementation of semi-Lagrangian advection schemes in the light of the results obtained.

2. THE LABORATORY BENCHMARK

(a) Apparatus

The experimental systems used in the present study comprise essentially the same two rigs as described by H85, though with some minor changes of instrumentation. Both annuli have the same dimensions and used the same working fluid, but were of differing construction and instrumentation. Velocity measurements were made in one rig (System A) via a particle-tracking method at five levels in the vertical spanning the entire depth of the apparatus, by illuminating a suspension of neutrally-buoyant polystyrene beads of approximate diameter 400-600 μm from the side through thin horizontal transparent inserts, and observing their horizontal motion using a CCTV camera mounted in the rotating frame. A second annulus (Rig B) was designed to measure temperatures within the flow (at an array of copper-constantan thermocouples, regularly-spaced in azimuth at mid-height and mid-radius), and to measure the total heat transport across the annular domain by a form of time-resolved calorimetry.

The details of the apparatus construction are given in H85, and the main parameters are shown in Table 1. A schematic diagram of the velocity measurement apparatus is reproduced in Fig. 1. The inner and outer boundaries comprise smooth brass cylinders, whose temperatures are maintained by circulating water (at a closely maintained initial temperature) through spiral channels adjacent to each sidewall at flow rates ~ 50 cm^3 s^{-1}. The horizontal boundaries consisted of insulating acrylic surfaces in contact with both surfaces of the working fluid. Wall temperatures were maintained stable to typically ± 0.01 K, with vertical variations of less than 2 % of the total temperature contrast in the system except at the outer wall of Rig A, where variations up to $\pm$ 3.5 % were obtained. The annuli were levelled to within 10^{-4} radians and centred on turntables with long term stability of around 1 part in 10^4. Heat transport measurements were made in the way described by Hignett (1982) and H85, from the temperature rise and flow rate of water circulating through the inner cylinder.

The working fluid was a mixture of glycerol in water (roughly 17 % by volume), whose density was adjusted to render the polystyrene beads used for flow visualisation and velocity measurement

neutrally-buoyant at approximately 20 °C. The main properties of this fluid, which was essentially the same in all cases as used in the 'main comparison' of H85, are summarised in Table 1.

(b) Data acquisition and analysis

(i) Temperature measurements. These were carried out as described by H85, indeed several of the cases to be used here for the model verification were taken from the the same study. Temperatures were measured at mid-level and mid-depth from a ring of 32 thermocouples, equally-spaced in azimuth. Fourier analysis of these measurements enables the amplitude and phase of each azimuthal harmonic of the temperature field to be obtained at regular intervals. Time-averaged spectra and time- variations in wave amplitudes were obtained in the manner described by H85.

By careful calibration of the temperature and flow rate sensors, heat transport could be measured to an absolute precision of around ± 2 %. The design of the coolant system, with fairly high flow rates and small volume of the spiral channels adjacent to the sidewalls, resulted in a relatively short time-constant (~ 10-20 s) for the heat transport measurements, so that variations of heat transport e.g. during a vacillation cycle, could be measured.

(ii) Velocity measurements. The velocity measurement approach is essentially non-intrusive, in contrast to the temperature measurements, and therefore very suitable for quantitative comparisons with numerical simulations which do not contain mechanical obstacles. Horizontal velocity measurements were made at heights in cm above the base of 1.6, 4.3, 7.0, 9.7 and 12.4, in images which typically contained between 150-400 particles. The main difference between the methods adopted here and those of H85 are in the analysis of the velocity fields. In the present work, velocity measurements are processed to represent each component of the field as an azimuthal Fourier series, in which the horizontal spatial variation of each zonal wavenumber m component is expressed as a function of the form

$$u_{m,n}(r,\theta) = U_{mn}(b/r)^{1/2} \sin n\pi x \; e^{im\theta} \tag{3}$$

(where $x = (r-a)/(b-a)$) and each complex coefficient $U_{m,n}$ is computed from the set of raw measurements via a least-squares method (Bell 1984; Bell & Jackson 1985). This approach offers several advantages over the earlier methods used by H85 in using a set of radial eigenfunctions which are mutually orthogonal, and therefore amenable to fitting to a well-posed unique solution.

3. NUMERICAL MODELS AND ADVECTION SCHEMES

(a) Baseline model

The main model used for the baseline simulations is essentially the same as used by H85. It solves the non-hydrostatic Navier-Stokes equations for the baroclinic flow of a Boussinesq liquid, together with corresponding continuity and thermodynamic equations, in cylindrical annular geometry on a rotating reference frame, the details of which may be found in H85. The model equations include representations of the reduced gravity and centrifugal terms, and temperature variations of density, molecular viscosity and thermal diffusivity are represented via simple quadratic functions to a precision of better than 1%.

Boundary conditions correspond to rigid, non-slip, isothermal sidewalls at $r = a, b$ and rigid, non-slip insulating endwall boundaries at $z = 0, D$, constituting an idealisation of the actual experimental system. The finite difference structure of the model resembles the Arakawa C grid in the horizontal, with similar staggering in the vertical. A stretched mesh is used in the r and z directions, in order to resolve economically Ekman and thermal boundary layers adjacent to the end- and side-walls. In contrast to H85, however, the present work employs a range of resolutions from $(16 \times 16 \times 64)$ points in (r, z, θ) up to $(32 \times 32 \times 128)$ points in the 3D model, and up to (64×64) points in (r, z) in the 2D axisymmetric version of the model. Fig. 2 shows a typical grid for the 'standard resolution' adopted in the present work of (24×24) points in (r, z) and 64 points in θ.

The finite difference schemes employed were conventional conservative Eulerian methods which are formally second-order accurate on the non-uniform grid. The Piacsek & Williams (1970) scheme is used to represent advection of momentum, while advection of heat uses a flux form (Arakawa 1966, hereafter referred to as scheme E(A)), ensuring global conservation respectively of kinetic energy and mean temperature. Time integration uses a conventional leapfrog scheme with a Du Fort-Frankel representation of the diffusion terms, with smoothing applied every 21 timesteps. The pressure field at each timestep is determined from the solution of a Poisson equation, via a direct method due to Farnell (1980).

(b) Semi-Lagrangian variants

In the present work, a central objective was to evaluate several forms of semi-Lagrangian advection scheme in the simulation of baroclinically unstable flow, with particular emphasis on (a) the importance of formal accuracy in the interpolation procedure, (b) conservation and transport properties, and (c) the representation of the baroclinic conversion in the energy budget (especially since semi-Lagrangian schemes do not generally satisfy formal conservation relationships). Since most of these objectives can be addressed within the context of heat transport, we have conducted a series of simulations in which a semi-Lagrangian advection scheme has been substituted for the Arakawa scheme in the advection of temperature in the model outlined above, whilst leaving the representation of momentum advection (and of molecular thermal diffusion) unchanged. Although this approach precluded evaluating the schemes at large Courant numbers, it enabled the model development to proceed without the extra coding complexities associated with the implementation of semi-Lagrangian advection of momentum in a vector form (e.g. Bates et al. 1990).

A range of schemes was implemented, sampling the set of schemes currently being considered by the UK Meteorological Office. The determination of the departure points $\mathbf{x_d}$ was carried out fully in 3D using the direct method of McGregor (1993), in which terms in the Taylor expansion were retained up to $O(\Delta t^3)$. Various approaches toward interpolation were investigated, including the split form suggested by Bates (1984) and Golding (1992). In this approach (designated hereafter 'scheme C'), the problem is approximated as a sequence of two or three 1D interpolations, with a corresponding reduction in computation time by a factor ~ 3 over the full tensor product form in this part of the code, though the accuracy of the interpolation is also reduced, with uncertain consequences. Also included are full 2D and 3D versions of the cubic-Lagrange ('scheme A') and quintic-Lagrange ('scheme B') tensor product forms, which were investigated in order to evaluate the importance of interpolation accuracy on the performance of the model.

4. TEST CASES AND BASELINE SIMULATIONS

In the following sections, we describe the particular cases of baroclinic flow in a rotating annulus which were selected for validation of the various simulations, and present results from high resolution simulations using the baseline Eulerian model described above for initial comparison. The rotating thermally-driven annulus is well known to exhibit a rich variety of different flow regimes, depending upon the imposed experimental conditions (mainly Ω and ΔT), ranging from steady axisymmetric flows to highly complex and disordered irregular regimes akin to 'geostrophic turbulence' (e.g. see Hide & Mason 1975). For the present purposes, it was considered desirable to choose a range of flows which were sufficiently complex and nonlinear to form a challenging test to the numerics, but not too complex in time and space to allow clear quantitative comparisons between simulations and experiments without requiring precise initialisation of simulations.

Earlier work (H85; White 1988) had suggested that even simulation of the axisymmetric regime was far from trivial if close quantitative agreement between simulation and experiment was required, particularly with regard to quantities such as the Nusselt number (a dimensionless measure of total heat transport, defined as

$$\mathrm{Nu} = H_{tot}/H_{con}, \tag{4}$$

where H_{tot} is the total heat transported through a cylindrical surface in the annulus and H_{con} is the heat transport which would be transported by thermal conduction alone in a material with the same thermal conductivity as the working fluid). In 3D, the accurate simulation of a steady, regular wave was chosen as the first test case and, for ease of comparison with previous work, the case studied by H85 was selected. Finally, it was noted by H85 that the transition from a steady wave to a periodic 'amplitude vacillation' as Ω is reduced had proved difficult for their generation of (relatively low resolution) model, and they were only able to obtain successful simulations of a very low wavenumber ($m = 2$) vacillation. Attempts to simulate a comparable transition from $m = 3$ had not met with success, despite clear evidence for the existence of such a transition in the laboratory. The transition to $m = 3$ amplitude vacillation was therefore considered a suitably challenging test case with which to evaluate a range of numerical schemes.

(a) Axisymmetric flows

Despite its simplicity, the steady axisymmetric flow regime at relatively low rotation rates has proved surprisingly difficult to simulate in quantitative detail, particularly with regard to the heat transport. White (1988) showed a range of simulations, using a version of the present Eulerian annulus model but without a stretched grid, which were able to capture the basic structure of the zonal and meridional circulation and temperature fields, but were subject to the development of a spurious roll-like instability near the inner cylindrical sidewall, especially at very low or zero Ω. This appeared to produce a minor perturbation in the flow structure in this region but, around $\Omega = 0$, had a strong effect on the total heat transport, increasing the Nusselt number in the simulations by around 50% compared with laboratory measurements. It was only in simulations at very high spatial resolution ($\geq 64 \times 64$ points in (r, z)) that this instability was sufficiently suppressed to result in a slow convergence towards the measured value of Nu.

In the present work, therefore, we consider as our baseline Eulerian simulations a sequence of axisymmetric runs at a resolution of 64×64 points in (r, z) *with a stretched mesh.* The latter proved significant in helping to suppress (though not entirely eliminate) the spurious roll instabilities more effectively than in the simulations with an evenly-spaced grid, and showed good convergence towards the laboratory measurements of Nu. Fig. 3a shows the effect of increasing resolution on the simulated Nusselt number for the baseline model with a stretched mesh at a typical value of $\Omega = 0.3$ rad s^{-1}, with the laboratory measured value shown for comparison. The values of Nu in the simulations are always greater than the laboratory value, but have clearly saturated by around a resolution of (48×48) points to a value which lies within the error band of the laboratory measurement.

The variation of Nu with Ω is illustrated in Fig. 3b, showing the characteristic decrease in Nu with Ω within the axisymmetric regime (cf Hide & Mason 1975; Hignett 1982) from around 11.5 at $\Omega = 0.0$ to 10.0 at $\Omega = 0.5$ rad s^{-1}. The full resolution numerical simulations reflect this trend quite well, to within the experimental error except at very low rotation rates. The latter exception is almost certainly associated with the mild development of spurious roll-like instabilities, as mentioned above (White 1988), which enhance the effective heat transport even at the highest accessible resolution. The final values of Nu for a series of cases from $\Omega = 0.1$ - 0.5 rad s^{-1}, also simulated at a resolution of (64×64) points in (r, z), are tabulated in Table 2, and show close agreement with the laboratory values to within their absolute uncertainty ($\simeq \pm 2.5\%$).

The azimuthal velocity fields for two typical rotation rates are shown in Fig. 4, in which frames

(c) and (f) were obtained from laboratory measurements using the particle-tracking system (Rig B). The vertical levels at which the velocity profiles were measured are indicated at the side of each frame. Frames (a), (b), (d) and (e) of Fig. 4 show the corresponding simulated fields of T and v at a resolution of (64 $\times$ 64) for comparison. Velocity structures are in quite good qualitative agreement, showing the concentration of the prograde zonal jet towards the top of the inner cylinder, though this is more pronounced in the simulation. This may reflect the limited resolution of the velocity measurements and the assumed truncation of the interpolating functions (in which n is arbitrarily restricted to $n \leq 6$; see Bell 1984). The simulated zonal jets are generally somewhat stronger than in the measurements by around 10%, which is somewhat greater than the uncertainty on the laboratory measurements themselves (around $\pm$ 5%). This would appear to suggest that the horizontal thermal gradient in the interior of the flow is somewhat too strong, and indicative of some residual deficiencies in the representation of total heat transport. The representation of the boundary conditions as perfectly conducting sidewalls and thermally insulating endwalls may also be somewhat questionable at this level of precision (see also (b) below). Some evidence of spurious roll instabilities is evident in Fig. 4(a) and (b) as a corrugation of the T and v contours near the inner cylinder, and appear to be a fairly common occurrence in simulations at low rotation rates. The effects of these rolls are relatively weak in this simulation, however, and do not appear to influence the quantitative features of the flow too much. We may conclude, therefore, that the baseline simulations provide a reasonably accurate simulation of the laboratory system, though seem to require quite high spatial resolution to achieve full convergence.

(b) Steady regular waves

The simplest non-trivial three-dimensional flow useful for trial simulation in the rotating annulus is the steady wave, obtained as the initial baroclinic instability of the axisymmetric flow state reaches a stable equilibrium at moderate values of rotation rate and thermal contrast (Hide & Mason 1975). For the present purpose, we choose to use the case used by H85 in their comparison of laboratory measurements with a lower resolution version of the present Eulerian model, at ΔT = 4.0 K and $\Omega = 1.0$ rad s^{-1}, for which a well-proven set of experimental data exist on the thermal and velocity structure of the flow and the heat transport (and a new and more extensive set of velocity measurements was acquired specifically for the present study).

Fig. 5 shows a series of horizontal streamfunction fields from velocity measurements in the laboratory (computed using the method of Read 1991) alongside horizontal sections of pressure obtained from a simulation using the Eulerian model at a resolution of 24 × 24 × 64 points in (r, z, θ). The model is clearly seen to capture many details of the flow structure at each level, showing also that the pressure field acts as a very good approximation to the horizontal streamfunction in this highly geostrophic flow. The high degree of quantitative agreement between simulation and measurement (to a precision better than ± 5%) is further evident in Figs 6-8.

Fig. 6 shows a comparison of the measured time-averaged temperature amplitude spectrum (obtained by Fourier analysis of thermocouple measurements at mid-height and mid-radius) and volume- and time-averaged kinetic energy spectrum (obtained from horizontal velocity measurements) with the equivalent quantities from the simulation. Agreement between the temperature amplitudes of the dominant mode ($m = 3$) and its harmonics is generally good, though the simulation indicates a slightly larger amplitude (by around 5-10%) for the $m = 3$ and $m = 6$ components than the laboratory measurements, and somewhat smaller amplitudes at high wavenumbers. Non-harmonic components are generally much smaller in the simulation, almost certainly because of the relatively high level of measurement noise in the laboratory. Similarly, kinetic energy spectra show reasonable agreement for the main harmonic components and azimuthal-mean flow (with a general trend for the simulations to underestimate kinetic energy densities), but non-harmonic components in the laboratory are dominated by noise.

The spatial structures of the mean zonal flow are shown in Fig. 7 and those of the $m = 3$ and $m = 6$ velocity components are illustrated in Fig. 8, both of which show radial profiles at each of the five levels measured in the laboratory. The $m = 3$ and $m = 6$ components clearly agree to $\sim$ 10% over almost the whole of the domain measured in the laboratory, while the mean zonal flow

exhibits a clear double-jet pattern at each level, characteristic of other studies of the steady wave regime in this kind of system (H85), with agreement in magnitude to $\sim 5\%$ throughout.

Other quantities amenable to quantitative comparison include the mean Nusselt number. Some significant disagreement between the laboratory measurement of 9.20 ± 0.18 and the numerical simulation was reported by H85, who obtained a value of 10.45 ± 0.01 evaluated at each sidewall in a simulation with somewhat coarser resolution ($16 \times 16 \times 64$) than in the present work. In our case, however, disagreement is actually somewhat worse with respect to the laboratory measurement, with a value of 10.89 ± 0.02 at both sidewalls (although the system had not fully settled to its final state after 1000s of simulation, but showed a damped oscillatory behaviour apparently converging upon the value given above). This discrepancy was also noted by H85, though they did not offer any clear explanation. It is perhaps noteworthy, however, that the thermal diffusivity of the working fluid in the experiment does not differ strongly from that of the perspex used for the endwalls ($\kappa_{perspex} \simeq 1.1 \times 10^{-3}$ cm^2 s^{-1}), with the possible result that the endwalls do not act quite like a perfect insulator. The quantitative impact of this on the effective radial heat transport should perhaps be investigated further in future work.

Wave pattern drift rates were also discussed by H85. In the present simulation, the $m = 3$ wave component was observed to have a drift frequency of 7.40×10^{-3} rad s^{-1}, which compares quite well with the laboratory value of 7.8×10^{-3} rad s^{-1} with a repeatability spread of around 10 %, and that of the earlier (low-resolution) simulation of H85, indicating that our baseline model provides a good overall simulation of the regular steady wave flow for comparison with other methods.

(c) Transition to periodic amplitude vacillation

As the rotation rate is reduced from the steady wave state, the regular steady wave in the laboratory is typically observed to undergo a bifurcation to a time-dependent state in which the amplitude and drift rate of the dominant wavenumber m component and its harmonics exhibit a periodic modulation, often termed 'amplitude vacillation' (Pfeffer et al. 1980; Hignett 1985). The strength of this modulation and its period gradually increase as Ω decreases, until the flow gives way to a relatively steady flow with dominant wavenumber $m-1$. Recent work also suggests that the final transition may be preceded by a more complex multi-mode regime in which both m and $m-1$ components are present and interact in a chaotic nonlinear mode competition (e.g. Read et al. 1992).

H85 reported a successful simulation of $m = 2$ amplitude vacillation using their low resolution model, though were unable to simulate the equivalent behaviour at $m = 3$. Upon integrating the current baseline model at the same resolution while gradually reducing Ω from the steady wave state discussed in Section 4b, the model retained a roughly steady $m = 3$ state well beyond the value of Ω at which the laboratory flow was observed to make its transition to $m = 2$ via a large-amplitude vacillation. It was only upon reaching a critical value of around $\Omega = 0.70$ rad s^{-1} (corresponding to a value of thermal Rossby number $\Theta = g\alpha\Delta TD/[\Omega^2(b-a)^2 \simeq 1.06$) that the simulated flow began to exhibit a discernible amplitude vacillation. When Ω was further reduced to 0.65 rad s^{-1} ($\Theta \simeq 1.23$) the flow made a rapid transition to a steady $m = 2$.

When the present baseline model was run at higher resolution, however, a different (and more realistic) behaviour was observed. Fig. 9 shows the mean volume-integrated kinetic energy per unit mass and its standard deviation as a function of the thermal Rossby number Θ, obtained from measurements of velocity in the laboratory and from a baseline simulation at a resolution of 24 $\times$ 24 $\times$ 64 points in (r, z, θ) averaged over time intervals of 1500s. The laboratory measurements show an rms spread of around $\pm$ 5 % in the total kinetic energy for all values of $\Theta \leq 0.675$, representing the overall level of measurement uncertainty on this quantity. Pronounced amplitude oscillations with a period of $\sim$ 190s set in around $\Theta \simeq 0.7$, at which point the rms variation increased to around $\pm$20%. The strength of the oscillations continued to increase, and the period lengthened slightly, as Θ was increased further, reaching $\sim \pm 60\%$ of the mean value of 14.6 cm^5 s^{-2} and a period of $\simeq$ 240s around $\Theta = 0.87$ before the $m = 3$ component collapsed and was then replaced by a strong steady $m = 2$ flow.

The corresponding simulation reflected several aspects of this qualitative progression quite

well, and exhibited the onset of a periodic amplitude vacillation around $\Omega = 0.85$ rad s^{-1} with a period of 190 ± 3 s. The strength of this vacillation increased steadily as Θ increased, and the period lengthened to around 230s at $\Omega = 0.775$ rad s^{-1}. The simulation did, however, retain the $m = 3$ flow somewhat beyond the limiting value of Ω indicated by the laboratory results, and did not make the transition to $m = 2$ until $\Omega = 0.725$ rad s^{-1} ($\Theta \simeq 0.988$).

(d) Convergence of solutions?

The extent to which the simulated flow converges towards the actual flow in the laboratory with increasing spatial resolution is a question which should not be overlooked. The results presented above do suggest a noticeable improvement in the (already quite good) agreement between simulation and measurements obtained by H85 for axisymmetric and steady wave flows, by improving the spatial resolution from $(16 \times 16 \times 64)$ to $(24 \times 24 \times 64)$. This is particularly significant for simulating the onset and behaviour of $m = 3$ amplitude vacillation, which the lower resolution model fails to capture.

Some caution should be exercised, however, in extrapolating this apparently optimistic trend towards even higher resolution. The present baseline model has also been run at a resolution of $(32 \times 32 \times 128)$ under similar conditions to the sequence of simulations described above. In this case, the model produced no steady state, even at $\Omega = 1.0$ rad s^{-1}, but produced a sustained amplitude vacillation at all the rotation rates investigated ($1.0 \geq \Omega \geq 0.775$ rad s^{-1}), although the rms strength of this vacillation ($\pm$ 1.4 cm^5 s^{-2}) at $\Omega = 1.0$ rad s^{-1} was almost indistinguishable from that due to measurement uuncertainties in the laboratory data. The magnitude of this vacillation was, however, consistently at a significantly higher level than in the laboratory at $\Omega \geq 0.9$ rad s^{-1}. The baseline simulations presented above should therefore be treated with some caution as representing the fully converged numerical solution appropriate to this problem. Further progress towards a conclusive assessment of the ultimate convergence of our baseline model must await the possibility of simulations at even higher resolution, which were beyond the capabilities of our present systems.

5. SEMI-LAGRANGIAN SIMULATIONS: AXISYMMETRIC FLOWS

In the following sub-sections we examine a series of simulations of axisymmetric flows using a range of different advection schemes for the temperature field, mainly at a resolution of (24×24) and for each of the five rotation rates considered in Section 4a. The semi-Lagrangian simulations are compared with each other and with the Eulerian model at the same resolution, and with the full resolution Eulerian model and laboratory measurements discussed above in Section 4a.

(a) Bi-cubic interpolation in 2D

In the first series of semi-Lagrangian simulations, we consider cases using full 2D tensor interpolation (scheme A). A range of resolutions were investigated, from (16×16) up to (48×48) in a stretched mesh. Fig. 10 shows some representative temperature fields at two values of Ω (0.1 rad s^{-1}; Figs 10(a)-(d), and 0.5 rad s^{-1}; Figs 10(e)-(h)) at a resolution of (24×24). Figs 10(a) and (e) show the simulations using scheme A, while simulations using the Eulerian scheme E(A) at the same resolution and rotation rates are shown in Figs 10(d) and (h). Both scheme A and E(A) show no tendency for the spurious roll instabilities which were found in the high resolution E(A) simulation in Fig. 4(a), and produce results which, at first sight, look closely similar. Strong convective overshoot features are evident near the sidewall thermal boundary layers, especially at $\Omega = 0.1$ rad s^{-1}, and relatively weak thermal gradients occur near the top of the domain. Differences are apparent in the detailed form of the overshoot features, and more especially, in the vicinity of the lower Ekman layer, where a greater number of temperature contours appear to extend outwards from the inner wall with scheme A than with the E(A) simulations. There is also a slight indication of enhanced vertical and horizontal thermal gradients in the interior of the scheme A simulations.

The latter point is borne out by a comparison of the corresponding zonal velocity fields. Both scheme A and E(A) simulations show essentially the same qualitative features in v as was found in the high resolution E(A) runs in Fig. 4, though with some differences in magnitude. The velocity fields from scheme A were quite closely similar to those in Fig. 4(b) and (e), but were approximately 1-2% larger in amplitude, and hence were around 10-12% larger in amplitude than the laboratory measurements. The lower resolution E(A) simulations, however, produced zonal jets which were consistently around 20-30% weaker than those from scheme A, and hence around 10-15% weaker than the laboratory measurements under the same conditions. Scheme A simulations at higher resolution tend to show even stronger zonal jets, indicating a consistent trend towards overestimating horizontal thermal gradients.

The Nusselt numbers for the various axisymmetric simulations at this resolution are summarised in Table 3, and show some consistent trends between the different numerical schemes. For each of the semi-Lagrangian simulations it was necessary to examine the Nusselt numbers evaluated at the two sidewall boundaries separately (as indicated in Table 3) since, in contrast to the E(A) simulations, some significant differences were apparent. In the case of scheme A simulations, differences between $\mathrm{Nu}(r = a)$ and $\mathrm{Nu}(r = b)$ were no more than around $\pm$ 4% of the mean value at a resolution of (24×24), though this did vary somewhat with resolution. This almost certainly reflects small systematic departures from perfect conservation of heat in the simulations, since the basic form of scheme A does not satisfy formal any conservation relationship, again in contrast to the Eulerian E(A) scheme which conserves T at second order accuracy. The mean values of Nu for scheme A are generally 2-3% larger than for the E(A) simulations at the same resolution, which are themselves consistently around 1-2% larger than the corresponding laboratory measurements. The scheme A results are mostly within the 2.5% uncertainty of the laboratory measurements of Nu, indicating that scheme A shows a slight tendency to overestimate the advective heat transport, especially in the vicinity of the outer wall.

(b) Bi-quintic and split cubic schemes

In order to assess the sensitivity of the axisymmetric semi-Lagrangian simulations to the method of interpolation, two other parallel series of simulations were carried out using a full quintic tensor product scheme (scheme B) and the more economical split 2×1D approach suggested by Golding (1991; scheme C). The temperature fields from these simulations at a resolution of (24×24) are shown in Figs 10(b) and (f), and (c) and (g) respectively. The quintic scheme evidently produces fields which are consistently almost indistinguishable from scheme A, and show little or no sensitivity to the interpolation used at the boundaries. The split scheme C, however, shows some clear differences which indicate a significant degradation in the performance of the scheme in comparison with any of the others. The simulation at low rotation rate (Fig. 10(c)) is clearly subject to a quite severe boundary layer instability near the inner cylinder, which renders the flow unsteady and has a strong effect on the isotherm structure throughout the flow. The simulation at 0.5 rad s^{-1} is significantly improved, but shows some marked differences in isotherm structure from schemes A and B in the vicinity of the lower Ekman layer, around which the static stability is noticeably reduced with scheme C.

As one might expect from the above, the Nusselt numbers for scheme B simulations are closely similar to those from scheme A, differing by at most 0.2%, and indicate that the improved formal

accuracy of the quintic interpolation offers little quantitative advantage over scheme A in these cases. This is not the case for the split scheme C, however, which shows much larger differences in Nu between the inner and outer sidewall at this resolution. The spurious difference in Nu between sidewalls is a strong function of resolution for all schemes, but especially for scheme C. Fig. 11 shows the effect of varying resolution with scheme C from (16×16) to (48×48), indicating that at the highest resolution the two sidewalls are apparently in balance to around the uncertainty in the laboratory measurements of Nu.

6. SEMI-LAGRANGIAN SIMULATIONS: REGULAR BAROCLINIC WAVES

In the following sub-sections we examine a series of numerical simulations of the 3D cases outlined in Section 4, using the various semi- Lagrangian schemes discussed above. Section 6a discusses the simulation of an $m = 3$ steady wave using the tri-cubic scheme A for temperature advection and compares the results with corresponding laboratory measurements and the Eulerian E(A) simulations presented in Section 4. In Section 6b we consider the effects of replacing the semi-Lagrangian scheme with either scheme B or C, and in 6c we examine attempts to simulate the transition to $m = 3AV$ as Ω is reduced using all three semi-Lagrangian schemes.

(a) Steady $m = 3$ flow with tri-cubic scheme A

The model version using scheme A for temperature advection in all three dimensions was used to simulate a regular, steady $m = 3$ baroclinic wave flow at $\Delta T = 4.0$ K and $\Omega = 1.00$ rad s^{-1}, with otherwise identical parameters to the baseline E(A) simulations described in Section 4(b) and at a resolution of $(24 \times 24 \times 64)$ points in (r, z, θ). The 2D axisymmetric scheme A model was run to a steady state under identical conditions and resolution to provide an initial flow. The resulting temperature field was then perturbed with a weak $m = 3$ pattern plus a localised perturbation, and the full 3D scheme A model was run for a further 1000s with a timestep of 0.02s. During this period, the $m = 3$ perturbation grew and the flow equilibrated, and settled to an approximately steady state dominated by an $m = 3$ pattern which drifted in a prograde sense around the annulus.

(i) Temperature & KE spectra. The structures in velocity of the equilibrated flow pattern were largely similar to those obtained in the E(A) simulations shown above in Section 4, and we concentrate here upon the details of the simulated temperature field. Fig. 12a shows a composite of temperature amplitude spectra obtained at mid-height and mid-radius, as in Fig. 6a, showing the time-averaged wave amplitude spectra obtained from all the semi-Lagrangian simulations together

with the laboratory measurements and results from the E(A) (24×24×64) simulation. Like the E(A) simulation, scheme A is seen to produce a temperature field comprising $m = 3$ and its harmonics, with very weak amplitudes in other components. The amplitude of the dominant harmonic (0.278 K) is around 0.015K larger than the corresponding laboratory value, and around 0.005K smaller than the E(A) simulation at the same resolution. This is in contrast to the ($16 \times 16 \times 64$) E(A) simulation of H85, who obtained an amplitude $\sim$ 0.03K smaller than the laboratory case.

The $m = 6$ component with scheme A is significantly larger than the laboratory measurements by a factor $\simeq 2$, which is even greater than that obtained by the E(A) simulations (although H85 obtained fairly close agreement at their resolution), whereas at $m = 9$ all simulations seem to be in close agreement (to within the measurement uncertainty of 0.004 K) with the laboratory. For all higher harmonic components, however, both E(A) and scheme A simulations all seem to produce significantly lower amplitudes than in the laboratory (although the amplitude of $m = 15$ is rather close to the measurement noise level, and therefore quite uncertain).

In contrast, the kinetic energy spectrum from the scheme A simulation is in quite good quantitative agreement overall with the laboratory spectrum (Fig. 12b), especially for harmonic components $m = 6$, 9 and 12, for which discrepancies are only around $\pm$ 0.07 $cm^5\ s^{-2}$ or around 0.3% of the energy of the dominant $m = 3$ component. Very little energy appears in the non-harmonic components. The dominant wavenumber $m = 3$, however, is apparently significantly underestimated (11.9 $cm^5\ s^{-2}$ compared with 17.3 $cm^5\ s^{-2}$ in the laboratory).

Some possible reasons for significant discrepancies between laboratory measured temperature amplitude spectra and numerical simulations were discussed by H85. These included the possibility that the presence of the thermocouple ring might displace the location of the equivalent flow regime in parameter space, or that small errors in the positioning of the thermocouple ring might lead to significant systematic measurement errors in the presence of strong spatial gradients of temperature. The latter positioning errors would also lead to spurious spreading of amplitude into the non-harmonic components at amplitude levels comparable with the systematic errors in the main harmonics, though this does not seem to be strongly apparent in the spectra shown in Fig. 12. Assuming that most of the discrepancies are indeed a real effect, the main reason for them is most likely to derive from the properties of the numerical scheme itself. In this case, results would suggest that the semi-Lagrangian scheme tends to produce a slightly enhanced dominant component in temperature, a substantially enhanced first harmonic and broadly realistic amplitudes in the higher harmonics, though the kinetic energy response by the model is broadly consistent with the laboratory measurements apart from the dominant harmonic itself. This is in contrast to the E(A)

scheme, which results in a slightly larger dominant component in T and a weaker first harmonic (though both are still significantly enhanced relative to laboratory measurements) at comparable resolution.

(ii) Temperature fields Significant differences between the various numerical schemes are also apparent in the detailed structure of the simulated temperature fields within the wave. This is particularly apparent close to the critical level in the flow, where nonlinear effects associated with strong advection are especially significant. In the case of baroclinic waves in the rotating annulus with rigid, non-slip boundaries, the critical level is close to mid-height, around which one might expect to see evidence of filamentation and phenomena akin to vortex roll-up during the development and equilibration of the wave (e.g. see Bell 1994).

Figs 13a-c show the mid-level temperature field as simulated by the E(A) models at resolutions of $(16\times16\times64)$, $(24\times24\times64)$ and $(32\times32\times128)$. The high resolution field (Fig. 13c) clearly shows the presence of filamentary structures being drawn out of the thermal boundary layer adjacent to the inner sidewall and wrapping up into a 'cold pool' in the trough of each wave lobe. The equivalent structure is also apparent in the corresponding temperature field from the scheme A model shown in Fig. 13d, but at the standard resolution, and shows a distinct 'hook-like' feature extending outwards from the inner cylinder in the direction of the prevailing flow, though with less clear evidence for a well-developed 'cold pool'. A similar feature is also evident in the E(A) model at the standard resolution (Fig. 13b), but in this case the filamentary structures near the inner sidewall are somewhat more 'smeared out' and with some grid-lengthscale roughness in the field in the vicinity of the very strong thermal gradients near the inner cylinder itself. Such effects are even more apparent in the low resolution E(A) simulation (Fig. 13a), in which the filamentary structure is strongly 'smeared out', presumably by the effects of numerical diffusion (since all models use the same explicit molecular diffusion coefficients). On this basis, at least, the semi-Lagrangian scheme A would appear to show some significant advantages in representing thermal structures due to advection more faithfully at a given resolution than the comparable Eulerian scheme.

(iii) Nusselt numbers. The Nusselt numbers obtained by the scheme A model in the present regime are presented in Table 4, together with comparable values obtained using the other schemes. As was found for the axisymmetric flows, some significant differences occur between Nu evaluated at the inner and outer sidewalls for all the semi-Lagrangian schemes, though the difference is no greater than $\pm$ 2% for scheme A. The mean value of 11.37 is around 23% greater than the measured value of 9.2, and approximately 6% greater than the high resolution E(A) simulation, indicating a slight tendency, as found for the axisymmetric model, for scheme A to produce more vigorous

advective heat transport than for the E(A) scheme.

(iv) Energetic conversion rates. A further key property of the different numerical schemes is their effect upon the energetic exchanges within the simulated flows. In the present cases, this is of particular importance with regard to the conversion from potential energy to eddy kinetic energy, which is essentially determined by the vertical advection of temperature. In the present set of models, we make use of a form of energy budget deriving from that developed by James et al. (1981), in which the rate of change of the kinetic energy K_m of each zonal wavenumber m component (integrated thoughout the annular domain) is treated separately according to

$$\frac{dK_m}{dt} = P_m + N_m - D_m \tag{6}$$

where P_m represents the conversion of potential energy to kinetic energy at wavenumber m by convective overturning and sloping convection and is given by

$$P_m = -2\pi g\alpha \int_0^D \int_a^b (w_m T_m^* + w_m^* T_m) r dr dz \tag{7}$$

(where $()^*$ denotes the complex conjugate), D_m represents the dissipation of kinetic energy by viscosity and N_m results from nonlinear interactions with other wavenumbers. In the case of interactions involving the zonal mean $m = 0$ components, N_m effectively represents the barotropic conversion rate to eddy kinetic energy at wavenumber m. For the present purposes, we choose to divide the analysis so as to distinguish only between the zonal mean $m = 0$ component and all the waves, and obtain the latter by summing each term over $1 \leq m \leq m_{max}$, where m_{max} is the maximum zonal wavenumber corresponding to the Nyquist frequency of the discretized zonal grid. The resulting simplified energy budget is essentially equivalent to the one developed by Williams (1971) in the context of his simulations of baroclinic annulus waves in a Boussinesq liquid.

The results of such an analysis for the various simulations of steady $m = 3$ flow are summarised in Table 4, which lists the principal azimuthal mean and 'eddy' components of kinetic energy and conversion terms, averaged over the last 1000s of each simulation. The energy budget for each component in terms of the net kinetic energy tendency is found to balance to a high degree of precision (better than 1%), indicating that the analysis provides a good representation of the overall energetics of each quasi-steady flow. The eddy baroclinic conversion $P_{m>0}$ in the Eulerian

E(A) simulations typically corresponds to a growth rate for eddy kinetic energy of around 0.17 s^{-1}, though the magnitude of the term depends somewhat on the spatial resolution. The results in Table 4 show a general trend towards increased values of $P_{m>0}$ as resolution increases, which is also correlated with increased values of $K_{m>0}$ and K_0, though P_0 appears to decrease with increased resolution. The baroclinic conversion strongly dominates over the 'barotropic' conversion N_{0-m} by a factor ~ 6, which is consistently positive (i.e. with waves gaining kinetic energy at the expense of the zonal flow) in all simulations, while the viscous dissipation terms D_0 and $D_{m>0}$ adjust to compensate for other changes in the overall budget. The semi-Lagrangian scheme A simulation exhibits values of kinetic energy and conversion terms which are generally intermediate between the Eulerian E(A) results at resolutions of $(24 \times 24 \times 64)$ and $(32 \times 32 \times 128)$ respectively, except that $P_{m>0}$ is actually greater than for any of the Eulerian simulations. This would appear to reflect the enhanced level of activity in the temperature field produced by semi-Lagrangian advection, suggesting an enhancement of baroclinic activity by around 5-7% in the scheme A simulations over the corresponding Eulerian scheme.

(b) Steady waves: Tri-quintic and split cubic schemes

Two other cases were investigated at the same nominal point in parameter space as in (a) above, using both the semi-Lagrangian schemes B and C. Both cases were initialised as for scheme A from axisymmetric flows, each obtained from equilibrated simulations using the equivalent 2D models. Both cases resulted in an equilibrated quasi-steady flow dominated by a slowly-drifting $m = 3$ pattern.

The composite mid-radius/mid-height temperature spectrum (FIg. 12a) indicates that scheme B generates an even larger amplitude in the dominant wavenumber than for any other scheme, with a mean amplitude of 0.302 K; some 14% larger than the laboratory value. The first harmonic in the scheme B simulation is also very large, being around 2.5 times as large as found in the laboratory. The higher harmonics, however, are rather smaller in amplitude and, as found above for the E(A) and scheme A simulations, are generally smaller than the laboratory values. The spectrum from scheme C is rather different from the others, in having significant amplitude in the non-harmonic components (even compared with the laboratory measurements), suggestive of much stronger sideband activity than for any of the other simulations. This is also evident in the other components of the flow field, which show significant departures from three-fold rotational symmetry in the flow patterns from this simulation. The amplitude of the $m = 3$ component is around 20-30% smaller than in any of the other simulations and $\sim$ 12% smaller than the laboratory value, while

the higher harmonics are only a little smaller than the other simulations and comparable with the laboratory amplitudes (except for $m = 6$, for which the laboratory value seems remarkably small in comparison with all the simulations).

The mid-level temperature structures for the scheme B and scheme C simulations are shown in Figs 13e and f respectively. Significant differences between these two simulations and the previous scheme A and E(A) cases are clearly apparent, especially in the region near the inner cylinder. The scheme B simulation shows a pronounced 'hook-like' structure drawn out from the inner thermal boundary layer, which is apparently in equilibrium as the wave drifts around the annulus, and which is marginally stronger than the equivalent feature produced by scheme A (cf Fig. 13d). In scheme C, this effect seems to have gone one stage further, in that the filament is drawn out of the inner boundary layer, around the trough of the wave, and almost returned to the inner cylinder at the other side of the wave lobe, enclosing a distinct temperature maximum close to the vertex of the trough itself. This would seem to indicate that both scheme B and scheme C result in an enhanced level of advective activity compared with scheme A and the E(A) schemes, with scheme C showing the strongest effect.

This apparent enhancement of advective transport is further apparent in the Nusselt numbers for these simulations, at least for the inner cylinder (see Table 4). The values of Nu for scheme B at both inner and outer cylinders agree to within $\pm 3\%$, with a mean value which is marginally greater than for scheme A. For scheme C, however, there is a considerable discrepancy between the two sidewalls, which significantly exceeds that expected from the axisymmetric cases at this resolution (see Fig. 11), about a mean value of around 10.1. This would seem to indicate that complex three-dimensional structure further degrades the accuracy of the scheme C simulation, at least regarding global heat transport.

The overall levels of kinetic energy in the scheme B simulation are generally greater than for scheme A (see Table 4), though are still somewhat less than found in the laboratory velocity measurements. In scheme C, however, the levels of eddy kinetic energy are considerably smaller, though the $m = 0$ component is larger. The eddy baroclinic energy conversion rate $P_{m>0}$ for scheme B indicates rather more vigorous release of potential energy with this scheme than for either of the other semi-Lagrangian simulations, while scheme C seems to produce the weakest level of baroclinic conversion (both $P_{m>0}$ and P_0) overall. As in the E(A) simulations, barotropic conversions (N_{0-m}) are consistently positive in all three cases, and around 0.5 $cm^5\ s^{-3}$, indicating that the waves have some mixed baroclinic/barotropic character at this parameter range though are predominantly baroclinic.

(c) Transition to $m = 3$ amplitude vacillation?

As described above, as Ω is decreased, the steady wave flow in the laboratory is observed to undergo a bifurcation to a periodically-modulated oscillatory state with a period of around 200s, and this behaviour was broadly simulated quite well by the E(A) model, provided the spatial resolution was adequate. Attempts were therefore made with all three semi-Lagrangian schemes to try to emulate this experiment by conducting a series of long simulations in which each model version was run for an interval of 1000-2000s at a given value of Ω, and then Ω was successively reduced and the simulation continued for a further period using the endpoint of the previous segment of the simulation as its initial state. This series of experiments was carried out until Ω reached a value of 0.75-0.70 rad s^{-1}, which was well beyond the point at which the laboratory flow made a transition to $m = 2$.

Despite ensuring that the flow was perturbed after each reduction in Ω, one of the most remarkable results of this series of experiments was that *none* of the three semi-Lagrangian schemes resulted in any significant level of amplitude vacillation, even down to the lowest values of Ω investigated. Scheme B did show the onset of some weak time-dependence around $\Omega = 0.775$ rad s^{-1}, though this was only really apparent in the higher harmonic components and had an unrealistic period of only $\simeq$ 100s. A weak hint of a similar kind of fast but very weak oscillation also became apparent in the scheme A simulation, but only at the lowest values of Ω, while the scheme C simulation showed a strong tendency for the emergence of strong sideband activity (i.e. in $m = 2$ and $m = 4$) as Ω was reduced.

The overall results of this series of experiments are summarised in Fig. 14, which shows the time-averaged levels of $m = 3$ kinetic energy and their standard deviations in the simulated flows from schemes A-C, together with the equivalent data from the sequence of laboratory measurements over the same range of Θ. All three semi-Lagrangian simulations were found to retain a quasi-steady $m = 3$ flow well beyond the point where both the laboratory flow and the medium and high resolution E(A) simulations developed a strong periodic vacillation, though at varying levels of mean kinetic energy in the $m = 3$ component.

Although the flow did experience some perturbation each time Ω was reduced, the possibility was considered that the flow in all the semi-Lagrangian simulations had settled into a spurious metastable steady state which might coexist with a more realistic periodically-modulated flow state outside a limited 'basin of attraction'. Accordingly, an experiment was run at $\Omega = 0.80$ rad s^{-1} in which the initial state was taken from the medium resolution E(A) simulation close to the

maximum of an amplitude vacillation cycle, and the scheme A model was subsequently integrated until transients had apparently decayed. In practice, the large-amplitude periodic modulation present in the E(A) simulation decayed away rapidly (within one vacillation period or so), to be replaced eventually by a fast, weak oscillation in zonal harmonics $m \geq 9$ (see Fig. 15a). This oscillation was not present in the original scheme A simulation (cf Fig. 15b), suggesting the coexistence of at least two attracting solutions at this point in parameter space, although neither of which seem to bear much resemblance to the corresponding flow actually observed in the laboratory.

7. DISCUSSION

In the work presented above, we have carried out a series of careful comparisons between several variants of semi-Lagrangian advection schemes applied to thermal advection, corresponding simulations using a more conventional Eulerian scheme, and verifying measurements in the laboratory. The cases investigated have ranged from simple steady, axisymmetric flows, steady regular equilibrated baroclinic waves, and a bifurcation sequence to a periodic time-dependent flow.

(a) Axisymmetric flows.

In the case of steady axisymmetric flow, the basic bi-cubic scheme A produced results which compared well both with the Eulerian E(A) simulations and with laboratory measurements, though did show a general trend towards enhanced levels of transport compared with both E(A) simulations and experiments. This would appear to suggest a significant systematic bias in the semi-Lagrangian family of schemes towards overestimating transport at around the 10% level, though there may be grounds for suspecting some additional contributing factors arising from the idealisation of the insulating boundary conditions in all the models. The improved formal accuracy of the bi-quintic scheme B resulted in values of Nu which appeared to show some improvement upon scheme A, which were also reflected in cleaner morphology in the temperature fields. Overall, however, scheme B did not seem to offer many strong practical advantages which would justify its additional computational expense, at least for the steady flows investigated. It was clear, however, that the reduced formal accuracy of the split cubic scheme C did result in serious quantitative and qualitative degradation of almost all simulations unless the model was run at much higher spatial resolution than for the other schemes. This would clearly seem to undermine the apparent economical advantage of this scheme in most practical situations.

The spurious apparent departure from proper conservation of heat in all three semi-Lagrangian

schemes evidently leads to a number of artifacts, including the appearance of significant differences in Nusselt number at the two sidewalls, though does not otherwise seem to result in serious consequences for the long- term stability of the simulation. The apparent departures from conservation could be improved by running the model at higher spatial resolution, though again at some increased computational cost. It would be of some interest in further work to investigate the effect of modifying the scheme A to force conservation, e.g. along the lines suggested by Priestley (1993), to see whether such a device is sufficient to recover global conservation properties characteristic of the present Eulerian E(A) simulations.

(b) Steady waves.

All schemes investigated seemed to be capable of producing reasonably successful quantitative simulations of the main comparison case of steady, regular baroclinic wave flow, at least at the 'standard resolution' adopted here of $(24 \times 24 \times 64)$. Both the tensor-product semi-Lagrangian schemes (A and B) appeared to generate higher levels of eddy kinetic energy and temperature amplitudes than any of the E(A) simulations, though all simulations seemed to be slightly deficient with respect to eddy kinetic energy (though, somewhat surprisingly, not with respect to temperature amplitudes, where scheme B produced unrealistically large amplitudes of the $m = 3$ and $m = 6$ components of the temperature spectrum). The split-cubic scheme C produced rather smaller levels of eddy kinetic energy than either of the tensor-product schemes, compatible with its relatively small baroclinic conversion rate compared with schemes A and B. The baroclinic conversion rates for *all* the semi-Lagrangian schemes, however, were found to exceed the conversion rates in the E(A) models, even though the latter produced levels of EKE which were scarcely different from those with schemes A and B. This appears to result from a balance with relatively smaller eddy dissipation rates in the E(A) simulations, though the detailed reasons for this are not clear.

The general tendency for enhanced levels of heat transport in all the semi-Lagrangian schemes was apparent in the simulated Nusselt numbers, which were generally greater for schemes A and B than for any of the E(A) simulations. Discrepancies between the two sidewalls were most pronounced for scheme C, for which the additional complexity of the three-dimensional flow lead to an increased difference between Nu at $r = a, b$ compared with the axisymmetric model. Again, departures from formal conservation did not appear to result in serious problems for the long-term stability of the simulation. The improved formal accuracy of the quintic interpolation scheme offered a marginal improvement on model performance, but this advantage was not compelling at moderate resolution. At low resolution, however, it was clear that the split scheme C was in se-

rious trouble, and failed to converge to a realistic flow state for spatial resolutions coarser than $(24 \times 24 \times 64)$, regardless of timestep.

(c) Time-dependent flows and spurious attractors?

The most remarkable result from the present series of simulations was the clear failure of any of the semi-Lagrangian schemes to capture the transition from steady to periodically vacillating $m = 3$ flow as Ω was reduced. This was made even more remarkable, given the evident success of the E(A) model in showing quite good quantitative agreement with the experimental behaviour, including the parametric conditions for the onset of vacillation, vacillation frequency etc., provided the spatial resolution was sufficient. The detailed reasons for the failure of the semi-Lagrangian simulations to capture this phenomenon are not clear, though it is perhaps significant that the amplitude vacillation phenomenon is highly baroclinic, and therefore quite sensitive to the representation of heat transport in the model. Its occurrence is also found experimentally to be sensitive to the Prandtl number of the fluid (Jonas 1981), being less prevalent in fluids with lower Prandtl number. This may be significant if numerical diffusion plays a role in the simulations, in which case one might speculate that our use of semi-Lagrangian advection for temperature only may modify (perhaps reducing?) the effective Prandtl number for the flow.

The appearance of spurious stability or instability in numerical models of nonlinear systems is increasingly becoming recognized as an important source of uncertainty in the study of such systems. It is well known, for example, that, for some numerical models of systems of ordinary differential equations, the use of too large a timestep may result in spurious instability or chaos (e.g. Lorenz 1989) or the spurious suppression of instability (e.g. Corless et al. 1991; Iserles 1990). Recent studies have also highlighted similar effects in some systems of coupled partial differential equations (e.g. Moore et al. 1991; Yee et al. 1991), which have exposed sensitivities both to the space and time step lengths and to the numerical scheme itself. Although no systematic investigation of the effect of varying resolution and timestep was carried out in the present study, a few semi-Lagrangian runs in the region where amplitude vacillation was expected were carried out with shorter timesteps, though with no appreciable difference in behaviour. The present work would therefore seem to suggest that the semi-Lagrangian schemes investigated here may fall into the latter category associated with the scheme itself, and this question clearly needs to be addressed more carefully in future work.

(d) Further studies

The present investigation has highlighted a number of aspects of the simulation of rotating, stratified flow which are clearly sensitive to the representation of heat transport. In any future extension of this work, it would be highly desirable to look more closely at the sensitivity of the semi-Lagrangian simulations to enhanced resolution. It would also be desirable to implement semi-Lagrangian schemes for the representation of momentum transport in the model as well as for heat, in order to investigate whether mixing schemes in this way affects e.g. the effective Prandtl number as suggested above. Furthermore, given such a capability, the model would no longer be constrained by the CFL criterion in the choice of timestep, and it would then be possible to study the performance of the scheme at much larger Courant numbers, closer to values intended for operational use in atmospheric models (since without achieving large Courant numbers, the economical advantages of semi-Lagrangian advection are rather less apparent). Given the points raised in (c) above, however, the possibility that the use of such large timesteps might lead to an enhanced occurrence of spurious numerical artifacts should be considered seriously.

The particular cases of laboratory phenomena simulated in this (and previous) studies have clearly proved a challenging test for the range of numerical schemes under consideration - perhaps more challenging than one might have expected. It was decided at an early stage to focus on phenomena for which baroclinic effects were paramount, but clearly in atmospheric flows barotropic and other kinds of instability are also dominant under some circumstances. In the context of the thermally-driven annulus experiments, a comparable test of model performance where both baroclinic *and* barotropic effects are important may be found in the so-called 'structural vacillation' regime at higher values of Ω than considered in the present work (e.g. Hide & Mason 1975; Pfeffer et al. 1980; Read et al. 1992). This form of time-dependence is generally believed to result from the barotropic instability of the basic large-scale baroclinic wave pattern, in a manner analogous to the stability of Rossby waves, and forms a transitional regime along the way towards the emergence of fully-developed geostrophic turbulence. An investigation of the 'structural vacillation' regime should therefore certainly feature in any future evaluation of numerical schemes used for momentum advection.

ACKNOWLEDGEMENTS

It is a pleasure to thank past colleagues of the Geophysical Fluid Dynamics Laboratory of the Meteorological Office for making available apparatus, data and the baseline models for use in this investigation. Particular thanks are due to Drs P. Hignett and A. A. White and Mr W. D. N. Jackson. This work was carried out under Meteorological Office Contract MET 2a/0541, and in this context we are grateful to Drs M. J. P. Cullen and T. Davies of the Forecasting Research Division of the Meteorological Office for advice and encouragement during the project and to Drs B. Golding and M. H. Mawson for making their semi-Lagrangian code available to us and for providing further help and advice.

REFERENCES

Arakawa, A. 1966 Computational design for long term numerical integration of the equations of fluid motion. Two-dimensional incompressible flow, Part 1. *J. Comp. Phys.*, **1**, 119-143.

Bates, J. R. 1984 An efficient semi-Lagrangian and alternating directions implicit method for integrating the shallow water equations. *Mon. Wea. Rev.*, **112**, 2033-2047.

Bates, J. R., Semazzi, F. H. M., Higgins, R. W. and Barros, S. R. M. 1990 Integration of the shallow-water equations on the sphere using a vector semi-Lagrangian scheme with a multigrid solver. *Mon. Wea. Rev.*, **118**, 1615-1627.

Bates, J. R., Moorthi, S. and Higgins, R. W. 1993 A global multilevel atmospheric model using a vector semi-Lagrangian finite-difference scheme. Part I: Adiabatic formulation. *Mon. Wea. Rev.*, **121**, 244-263.

Bell, M. J. 1984 The least squares method of Fourier analysing two-dimensional velocity data produced by the Video Velocity Acquisition System. *Meteorological Office, Internal Report Met O 21 IR/84/6.*

Bell, M. J. 1992 The nonlinear evolution of a slowly growing wave on a laterally sheared baroclinic flow. *J. Fluid Mech.*,**241**, 615-643.

Bell, M. J. and Jackson, W. D. N. 1985 Further analysis of methods for fitting fields to two-dimensional velocity data. *Meteorological Office, Internal Report Met O 21 IR/85/1*

Corless, R. M., Essex, C. and Nerenberg, M. A. H. 1991 Numerical methods can suppress chaos. *Phys. Lett.*, **157**, 27-36.

Côté, J. and Staniforth, A. 1990 An accurate and efficient finite-element global model of the shallow water primitive equations. *Mon. Wea. Rev.*, **118**, 2707-2717.

Cullen, M. J. P., Davies, T., Mawson, M. H., Jones, J. A., Coulter, S. C. & Malcolm, A. 1994 Some issues in numerical methods for the next generation of NWP and climate models. *Meteorological Office, FR Scientific Note no. 26.*

Farnell, L. 1980 Solution of Poisson equations on a non-uniform grid. *J. Comp. Phys.*, **35,** 408-425.

Golding, B. W. 1992 An efficient non-hydrostatic forecast model. *Meteorol. Atmos. Phys.*, **50,** 89-103.

Hide, R. and Mason, P. J. 1975 Sloping convection in a rotating fluid. *Adv. in Physics*, **24,** 47-100.

Hignett, P. 1982 A note on the heat transfer by the axisymmetric thermal convection in a rotating fluid annulus. *Geophys. Astrophys. Fluid Dyn.*, **19,** 293-299.

Hignett, P. 1985 Characteristics of amplitude vacillation in a differentially-heated rotating fluid annulus. *Geophys. Astrophys. Fluid Dyn.*, **31,** 247-281.

Hignett, P., White, A. A., Carter, R. D., Jackson, W. D. N. and Small, R. M. 1985 A comparison of laboratory measurements and numerical simulations of baroclinic wave flows in a rotating cylindrical annulus. *Quart. J. R. Met. Soc.*, **111,** 131-154.

Iserles, A. 1990 Stability and dynamics of numerical methods for nonlinear ordinary differential equations. *IMA J. Num. Anal.*, **10,** 1-30.

James, I. N., Jonas, P R. and Farnell, L. 1981 A combined laboratory and numerical study of fully developed steady baroclinic waves in a cylindrical annulus. *Quart. J. R. Met. Soc.*, **107,** 51-78.

Jonas, P. R. 1981 Some effects of boundary conditions and fluid properties on vacillation in thermally-driven rotating flow in an annulus. *Geophys. Astrophys. Fluid Dyn.*, **18,** 1-23.

Leslie, L. M. and Purser, R. J. 1991 High-order numerics in an unstaggered three-dimensional time-split semi-Lagrangian forecast model. *Mon. Wea. Rev.*, **119,** 1612-1623.

McDonald, A. and Bates, J. R. 1989 Semi-Lagrangian integration of a gridpoint shallow-water model on the sphere. *Mon. Wea. Rev.*, **117,** 130-137.

McDonald, A. and Haugen, J. E. 1992 A two time-level, three-dimensional semi-Lagrangian, semi-implicit, limited-area gridpoint model of the primitive equations. *Mon. Wea. Rev.*, **120,** 2603-2621.

McGregor, J. L. 1993 Economical determination of departure points for semi-Lagrangian models. *Mon. Wea. Rev.*, **121**, 221-230.

Moore, D. R., Weiss, N. O. and Wilkins, J. M. 1990 The reliability of numerical experiments: transitions to chaos in thermosolutal convection. *Nonlinearity*, **3**, 997-1014.

Piacsek, S. A. and Williams, G. P. 1970 Conservation properties of finite difference schemes. *J. Comp. Phys.*, **6**, 392-405.

Pfeffer, R. Buzyna, G. and Kung, R. 1980 Time-dependent modes of behavior of thermally-driven rotating fluids. *J. Atmos. Sci.*, **37**, 2129-2149.

Purser, R. J. and Leslie, L. M. 1988 A semi-implicit semi-Lagrangian finite-difference scheme using high-order spatial differencing on a nonstaggered grid. *Mon. Wea. Rev.*, **116**, 2069-2080.

Priestley, A. 1993 A quasi-conservative version of the semi-Lagrangian advection scheme. *Mon. Wea. Rev.*, **121**, 621-629.

Read, P. L. 1990 Determination of streamfunctions and velocity potentials using analysed velocity fields from VVAS data. *Meteorological Office, Met O 21 Internal Report IR89/1.(revised 1990).*

Read, P. L., Bell, M. J., Johnson, D. W. and Small, R. M. 1992 Quasi-periodic and chaotic flow regimes in a thermally-driven, rotating fluid annulus.*J. Fluid Mech.*, **238**, 599-632.

Ritchie, H. 1991 Application of the semi-Lagrangian method to a multilevel spectral primitive-equations model. *Quart. J. R. Met. Soc.*, **117**, 91-106.

Ritchie, H. and Beaudoin, C. 1994 Approximations and sensitivity experiments with a baroclinic semi-Lagrangian spectral model. *Mon. Wea. Rev.*,

Robert, A. 1981 A stable numerical integration shceme for the primitive meteorological equations. *Atmos.-Ocean*, **19**, 35-46.

Robert, A. 1982 A semi-Lagrangian and semi-implicit numerical integration scheme for the primitive meteorological equations. *J. Met. Soc. Japan*, **60**, 319-325.

Robert, A., Yee, T. L. and Ritchie, H. 1985 A semi-Lagrangian and semi-implicit numerical integration scheme for multilevel atmospheric models. *Mon. Wea. Rev.*, **113**, 388-394.

Staniforth, A. and Temperton, C. 1986 Semi-implicit semi-Lagrangian integration schemes for a barotropic finite-element regional model. *Mon. Wea. Rev.*, **114**, 2078-2090.

Staniforth, A. and Côté, J. 1991 Semi-Lagrangian integration schemes for atmospheric models - a review. *Mon. Wea. Rev.*, **119**, 2206-2223.

Tanguay,M., Simard, A. and Staniforth, A. 1989 A three-dimensional semi-Lagrangian scheme for the Canadian regional finite-element forecast model. *Mon. Wea. Rev.*, **117**, 1861-1871.

Tanguay, M., Robert, A. and Laprise, R. 1990 A semi-implicit semi-Lagrangian fully compressible regional forecast model. *Mon. Wea. Rev.*, **118**, 1970-1980.

Temperton, C. and Staniforth, A. 1987 An efficient two-time-level semi-Lagrangian semi-implicit integration scheme. *Quart. J. R. Met. Soc.*, **113**, 1025-1039.

White, A. A. 1988 The dynamics of rotating fluids: numerical modelling of annulus flows. *Meteorol. Mag.*, **117**, 54-63.

Williams, G. P. 1971 Baroclinic annulus waves. *J. Fluid Mech.*, **37**, 727-750.

Williamson, D. and Rasch, P. 1989 Two-dimensional semi-Lagrangian transport with shape-preserving interpolation. *Mon. Wea. Rev.*, **117**, 102-129.

Williamson, D. L. and Olsen, J. G. 1994 Climate simulations with a semi-Lagrangian version of the NCAR CCM2. *Mon. Wea. Rev.*

Yee, H. C., Sweby, P. K. and Griffiths, D. F. 1991 Dynamical approach study of spurious steady-state numerical solutions of nonlinear differential equations. I. The dynamics of time discretization and its implications for algorithm development in computational fluid dynamics. *J. Comp. Phys.*, **97**, 249-

Figure Captions

Figure 1: Schematic sections through the rotating annulus used in the present study. The left-hand section represents the velocity measurement system, showing the approximate location of transparent acrylic inserts (indicated L) for illumination of tracer particles. The right-hand section illustrates the arrangement of fine-wire thermocouple probes (labelled T) at mid-height and mid-radius. Other labelled features are: A, insulating lid; B, insulating base; C, inner cylindrical sidewall; D, outer cylinder.

Figure 2: Layout of the principal grids in (r,z) and (r,θ) for the numerical model at the baseline resolution of (24 x 24 x 64) in (r,z,θ).

Figure 3: The variation of simulated Nusselt number in the axisymmetric flow regime using the Eulerian E(A) scheme (a) as a function of model resolution at $\Omega = 0.3$ rad s^{-1} and (b) as a function of Ω at a resolution of (64 x 64) in (r,z). The corresponding laboratory measurements are shown with appropriate error bounds for comparison.

Figure 4: Simulations of axisymmetric flow using the Eulerian E(A) scheme at $\Omega = 0.1$ rad s^{-1} (a-b) and $\Omega = 0.5$ rad s^{-1} (d-e), showing temperature fields ((a) and (d); contour interval 0.25 K) and azimuthal velocity ((b) and (e); contour interval 0.05 cm s^{-1}). Corresponding azimuthal velocity fields from laboratory measurements are shown in (c) and (f) for comparison at the same contour interval as (b) and (e).

Figure 5: Contour maps of horizontal streamfunction, derived from measurements of horizontal velocity in a steady m=3 flow in the laboratory ((a) - (c)) at three levels in the vertical, compared with maps of the pressure field (p/ρ) at the same three levels obtained in a numerical simulation at baseline resolution using the E(A) model at the same point in parameter space. Horizontal levels correspond to z/D = 0.89 ((a) and (d)), 0.50 ((b) and (e)), and 0.11 ((c) and (f)). Contour intervals are 0.05 cm^2 s^{-1} ((a)-(c)) and 0.1 cm^2 s^{-2} ((d)-(f)) - the latter corresponding to $\varphi = p/2\Omega r$ for $\Omega = 1.0$ rad s^{-1}.

Figure 6: Azimuthal wavenumber spectra of (a) temperature at mid-height and mid-radius, and (b) volume-integrated kinetic energy per unit mass, in a steady m=3 baroclinic flow. Data were obtained from laboratory measurements [T(lab)] and numerical simulations using the E(A) model at the baseline [T(DFF24)] (24 x 24 x 64) and high [T(DFF32)] (32 x 32 x 128) resolutions.

Figure 7: Radial profiles of azimuthal velocity in the steady m=3 flow for (a) the azimuthal mean flow component, (b) the m=3 wave and (c) m = 6 wave components, at the five vertical levels measured in the laboratory. Solid lines show the profiles obtained in the baseline (24 x 24 x 64) E(A) model simulation and dashed lines show the corresponding time-averaged profiles from laboratory measurements of horizontal velocity. Mean flow profiles are scaled in cm s^{-1}, m = 3 component profiles are scaled to a maximum velocity of 2.5 mm s^{-1} and m = 6 to 0.71 mm s^{-1}.

Figure 8: Radial profiles of radial velocity in the steady m=3 flow for (a) the m = 3 and (b) m = 6 wave components, at the vertical levels measured in the laboratory. Solid lines correspond to the profiles obtained in the baseline E(A) simulation and dashed lines show the corresponding laboratory measurements. The m = 3 component profiles are scaled to a maximum value of 2.2 mm s^{-1} and the m = 6 profiles to 0.63 mm s^{-1}.

Figure 9: The onset of m = 3 amplitude vacillation as Ω is reduced in small steps from 1.0 rad s^{-1}, as exhibited in the laboratory and in the baseline E(A) numerical simulation. Graph shows volume-integrated kinetic energy per unit mass for azimuthal wavenumber components m = 3 and m = 2 (KE3 and KE2) from velocity measurements in the laboratory, and the m = 3 component from the numerical simulation, as a function of thermal Rossby number Θ. 'Error bars' indicate the rms variability in kinetic energy at each value of Θ.

Figure 10: Temperature fields in the (r,z) plane from semi-Lagrangian and Eulerian simulations of axisymmetric flows at Ω = 0.1 rad s^{-1} [(a) - (d)] and 0.5 rad s^{-1} [(e) - (h)] at the baseline resolution of (24 x 24). Schemes used are semi-Lagrangian scheme A [(a) and (e)], scheme B [(b) and (f)], scheme C [(c) and (g)] and Eulerian scheme E(A) [(d) and (h)]. Contour interval is 0.25 K.

Figure 11: Convergence of Nusselt number at the inner and outer sidewalls in semi-Lagrangian scheme C simulations of axisymmetric flow at Ω = 0.3 rad s^{-1} with increasing resolution. Open squares show the Nusselt number at the outer boundary, filled diamonds show Nu at the inner boundary, and the solid line indicates the value of Nu measured in the laboratory.

Figure 12: Azimuthal wavenumber spectra of (a) temperature amplitude and (b) kinetic energy (cf Fig. 6), for semi-Lagrangian and baseline Eulerian model simulations of the steady m = 3 baroclinic wave flow. The values measured in the laboratory are shown as T(lab) and KE(lab) respectively for comparison.

Figure 13: Contour maps of temperature at mid-height in simulations of steady m = 3 baroclinic wave flow. Frames (a) - (c) are taken from Eulerian E(A) simulations at resolutions of (a) (16 x 16 x 64), (b) (24 x 24 x 64) and (c) (32 x 32 x 128). Frames (d) - (f) are taken from semi-Lagrangian simulations at the baseline resolution and correspond to (d) scheme A, (e) scheme B and (f) scheme C. Contour intervals are 0.05 K.

Figure 14: As for Fig. 9, but showing the variation of kinetic energy in the m = 3 component for semi-Lagrangian simulations using schemes A-C for comparison with the laboratory measurements. 'Error bars' again indicate rms variability over 1000s periods, though this is generally very small for all the semi-Lagrangian simulations.

Figure 15: Time series of kinetic energy in azimuthal wavenumber components m = 0, 3, 6, 9 and 12, taken from semi-Lagrangian scheme A simulations of m = 3 baroclinic wave flows at Ω = 0.80 rad s^{-1}, at which the laboratory flow exhibits a strong amplitude vacillation. Frame (a) shows the development of a weak periodic modulation of m = 9 and m = 12 following a perturbation of an otherwise steady wave flow (shown for comparison in frame (b)).

TABLE 1

Annulus Dimensions and Fluid Properties

Quantity	Symbol	Value	Units
Fluid depth	D	14.0	cm
Outer cylinder radius	b	8.00	cm
Inner cylinder radius	a	2.50	cm
Temperature difference	ΔT	4.0	K
Kinematic viscosity	ν	1.66×10^{-2}	$cm^2\ s^{-1}$
Thermal diffusivity	κ	1.27×10^{-3}	$cm^2\ s^{-1}$
Mean fluid density	ρ	1.044×10^{3}	$kg\ m^{-3}$
Volumetric expansion coefficient	α	2.86×10^{-4}	K^{-1}

TABLE 2

Nusselt numbers in axisymmetric flows as a function of resolution for Eulerian (DFF) model

Resolution	Omega (rad s^-1)					
	0.0	0.1	0.2	0.3	0.4	0.5
16 x 16		11.80	11.53	11.15	10.73	10.28
24 x 24		11.66	11.36	10.98	10.55	10.11
32 x 32		12.24	11.31	10.93	10.50	10.05
48 x 48		12.17	11.55	10.88	10.46	10.01
64 x 64		11.96	11.45	10.87	10.45	10.00
Laboratory	11.5	11.4	11.2	10.7	10.3	10.0

Table 3

Nusselt Numbers in axisymmetric flows for various numerical advection schemes (at 24 x 24 resolution)

	Omega (rad s^-1)				
Scheme	0.1	0.2	0.3	0.4	0.5
2D DFF	11.66	11.36	10.98	10.55	10.11
2D Cubic SL	11.65	11.30	10.87	10.41	9.95
	11.75	11.69	11.46	11.14	10.78
2D Quintic SL	11.67	11.31	10.88	10.42	9.94
	11.69	11.65	11.44	11.13	10.77
2 x 1D Cubic SL	12.39	11.99	11.50	10.93	10.39
	9.92	9.64	9.52	9.60	9.43
Laboratory	11.4	11.2	10.7	10.3	10.0

Table 4

Time-mean Nusselt numbers and energetic conversion rates for simulations of steady baroclinic waves

Numerical Scheme & resolution	Nu (a/b)	K_0	$K_{m>0}$	$P_{m>0}$	P_0	N_{0-m}	D_0	$D_{m>0}$
		($cm^5\ s^{-2}$)		($cm^5\ s^{-3}$)				
Eulerian E(A) (16 × 16 × 64)	10.98/ 10.97	4.60	12.62	2.25	6.82	0.43	-6.40	-2.70
Eulerian E(A) (24 × 24 × 64)	10.89/ 10.94	4.75	13.57	2.51	6.33	0.43	-5.90	-2.96
Eulerian E(A) (32 × 32 × 128)	10.71/ 10.74	5.35	14.28	2.60	6.21	0.41	-5.81	-3.02
Semi-Lag. Scheme A (24 × 24 × 64)	11.16/ 11.58	3.98	14.06	2.73	6.32	0.56	-5.77	-3.30
Semi-Lag. Scheme B (24 × 24 × 64)	11.10/ 11.71	4.20	14.85	2.89	6.30	0.54	-5.76	-3.45
Semi-Lag. Scheme C (24 × 24 × 64)	12.75/ 7.42	4.16	11.44	2.65	6.02	0.59	-5.43	-3.25

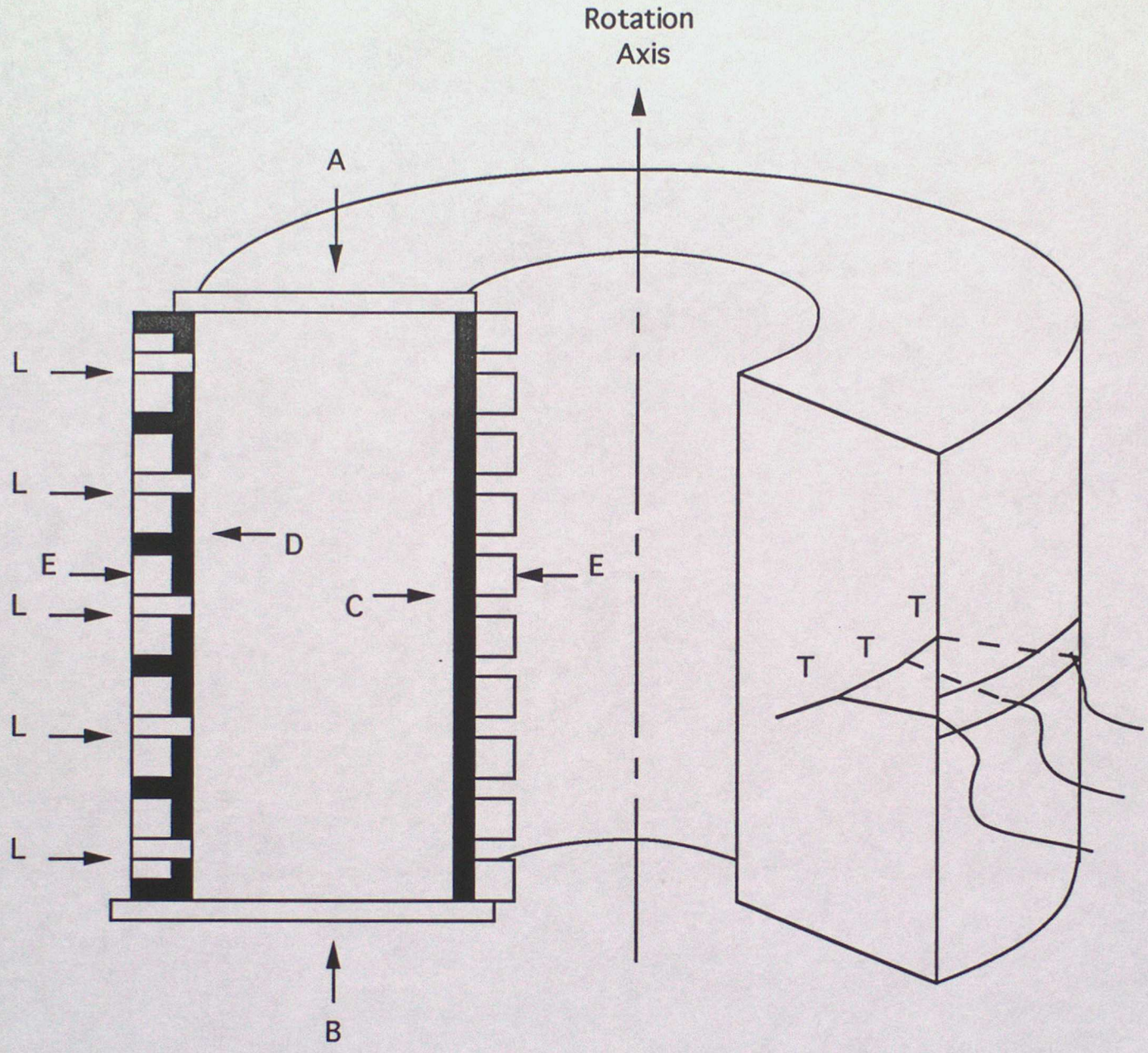

Fig. 1

Fig. 2

R - Z SECTION OF GRID POSITION

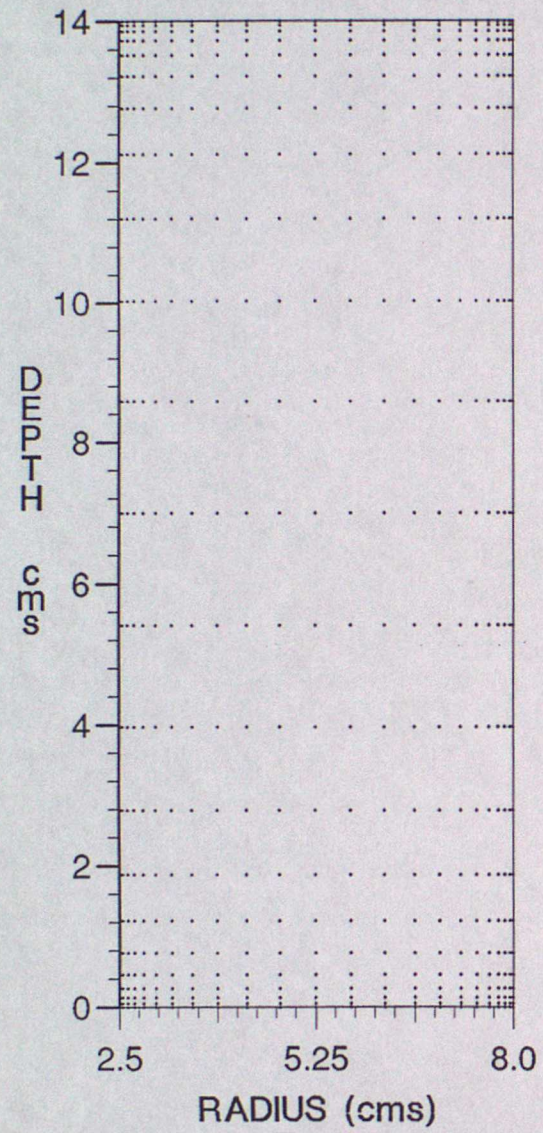

R-THETA SECTION OF GRID POSITION

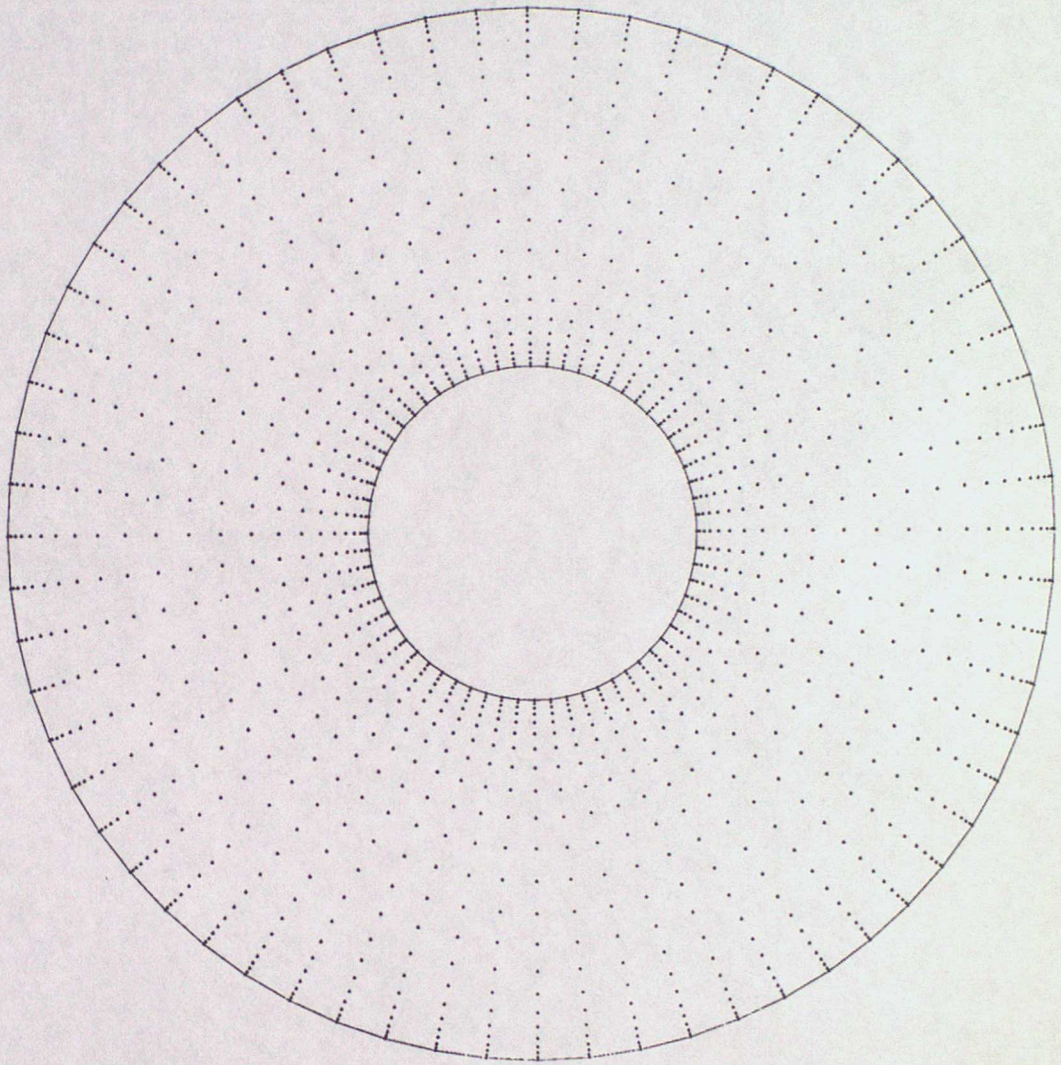

Fig 3

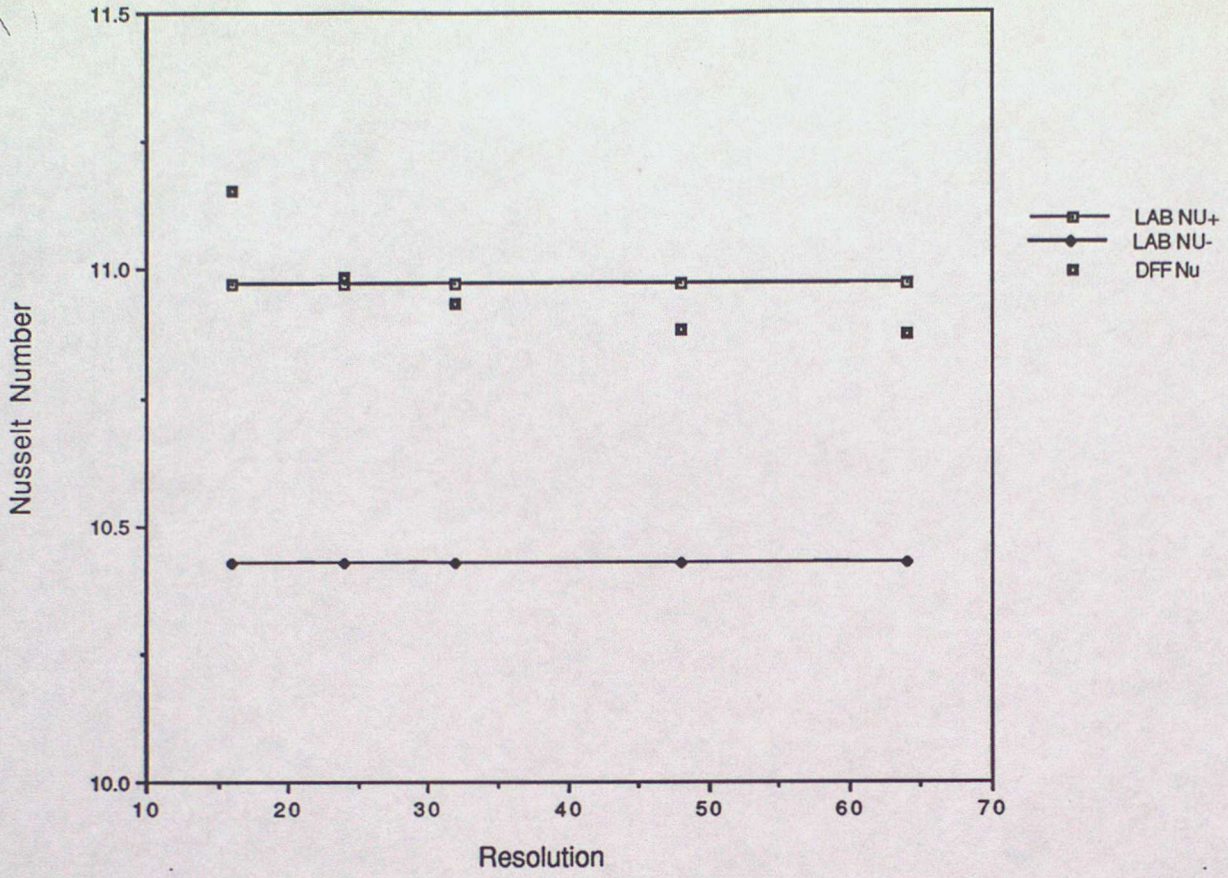
11.5
11.0
10.5
10.0
Nusselt Number
10
20
30
40
50
60
70
Resolution
LAB NU+
LAB NU-
DFF Nu

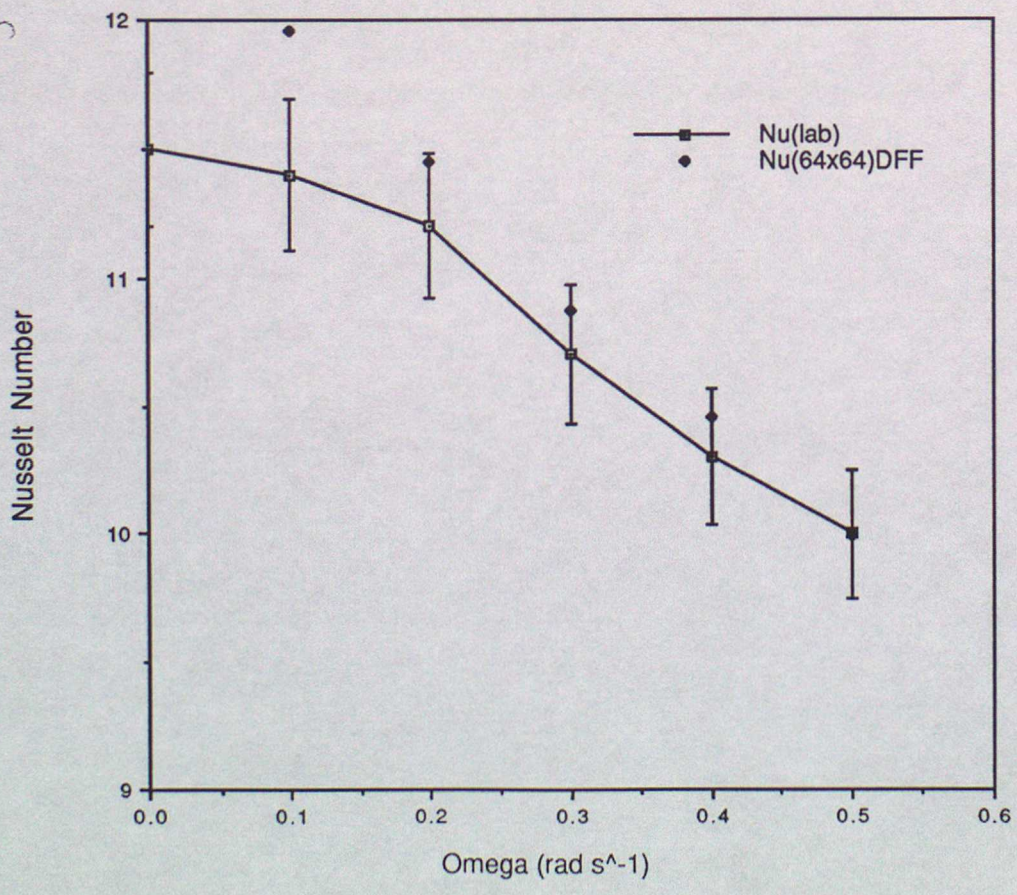
12
11
10
9
Nusselt Number
0.0
0.1
0.2
0.3
0.4
0.5
0.6
Omega (rad s^-1)
Nu(lab)
Nu(64x64)DFF

Fig 4

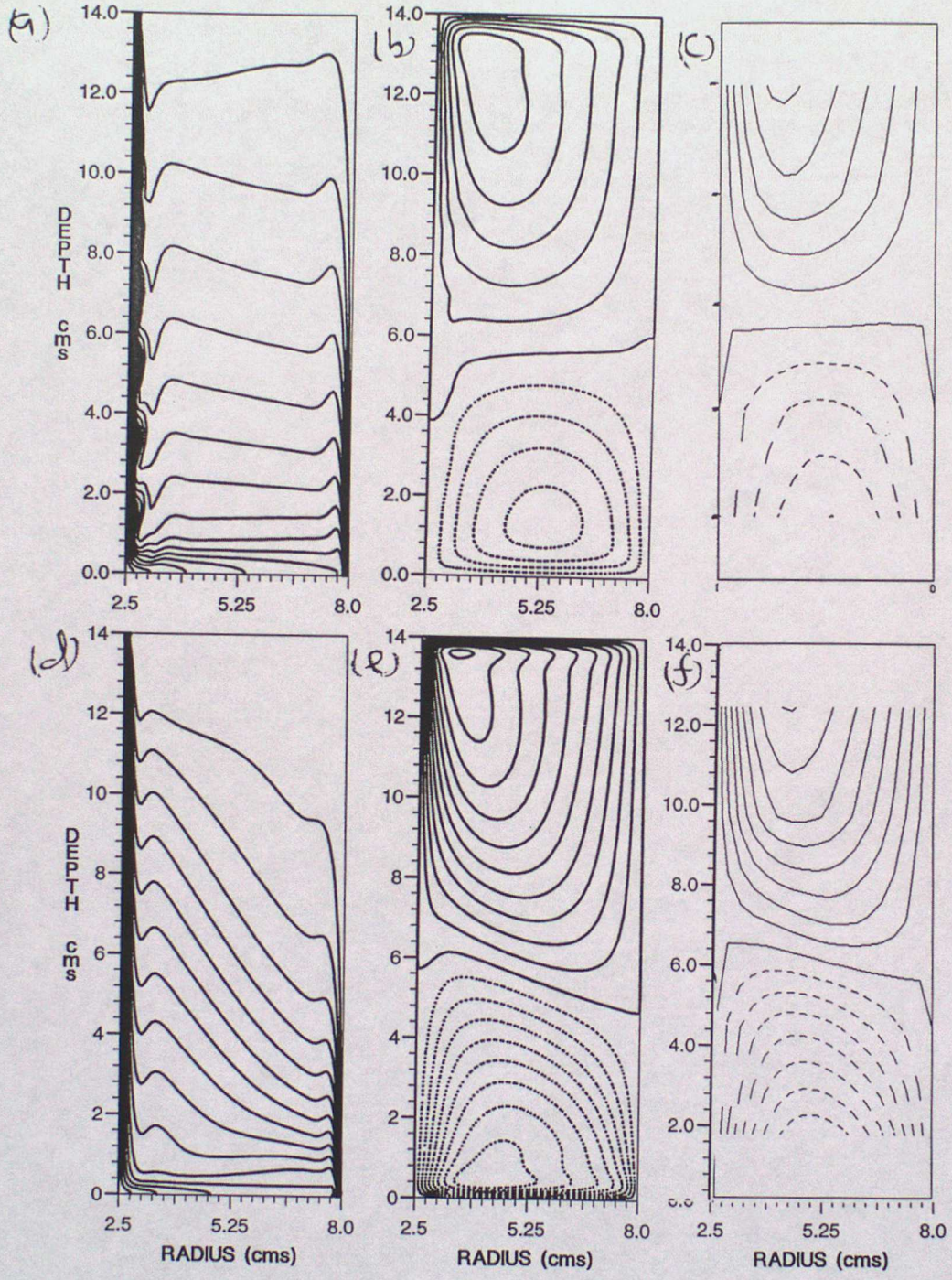

(a)
(b)
(c)
(d)
(e)
(f)

Fig 6

Data from "Steady wave spectra"

(a)

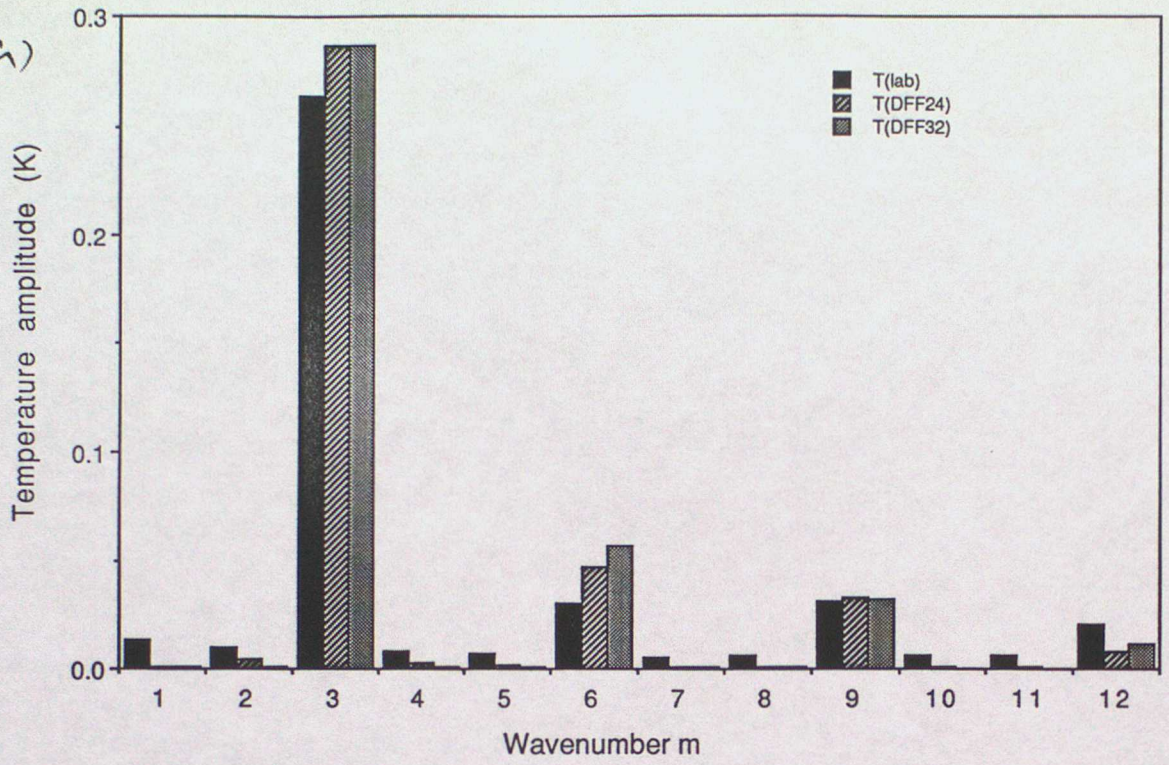

(b)

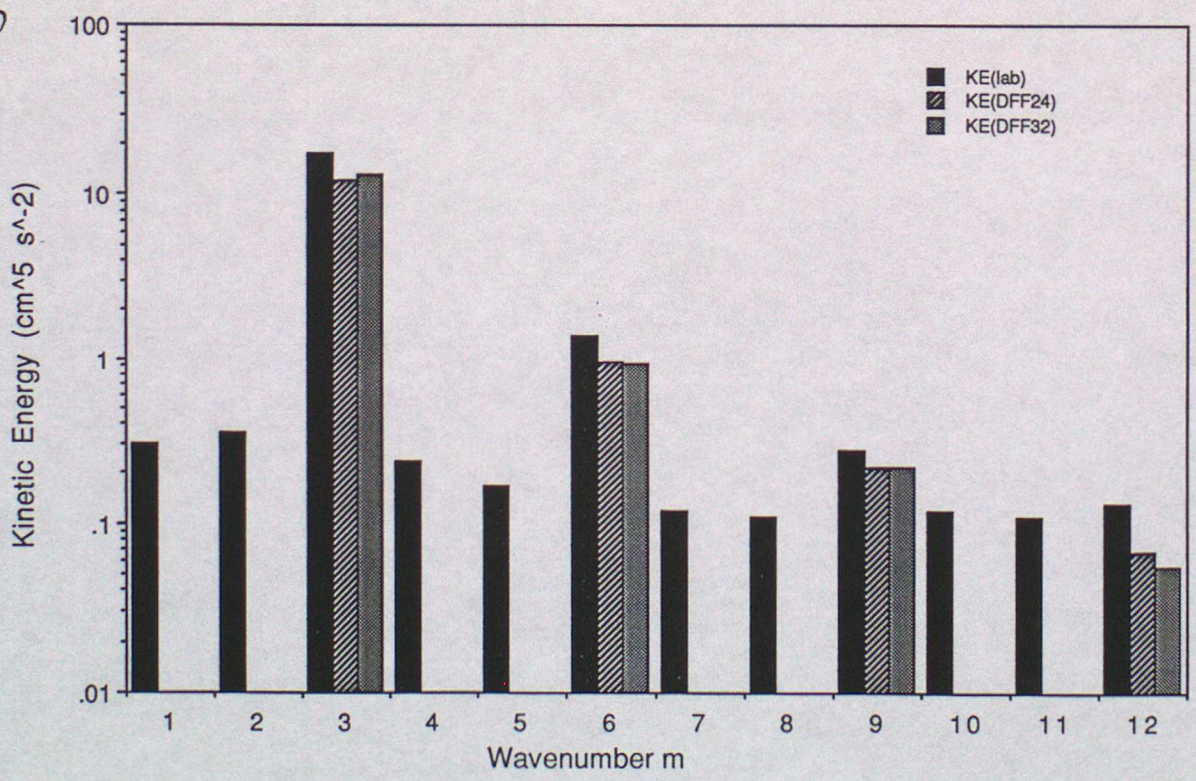

Fig 7

Fig 8

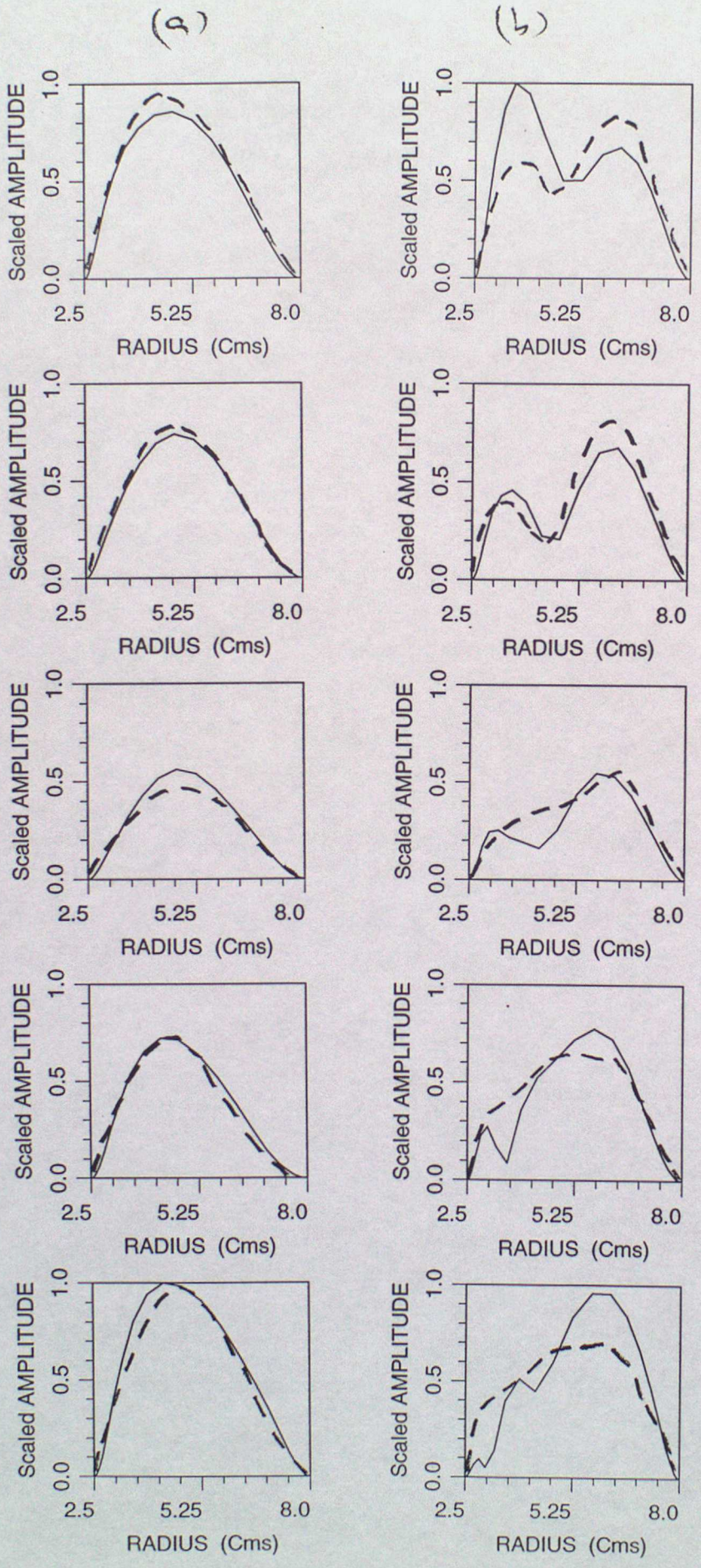

Fig. 9

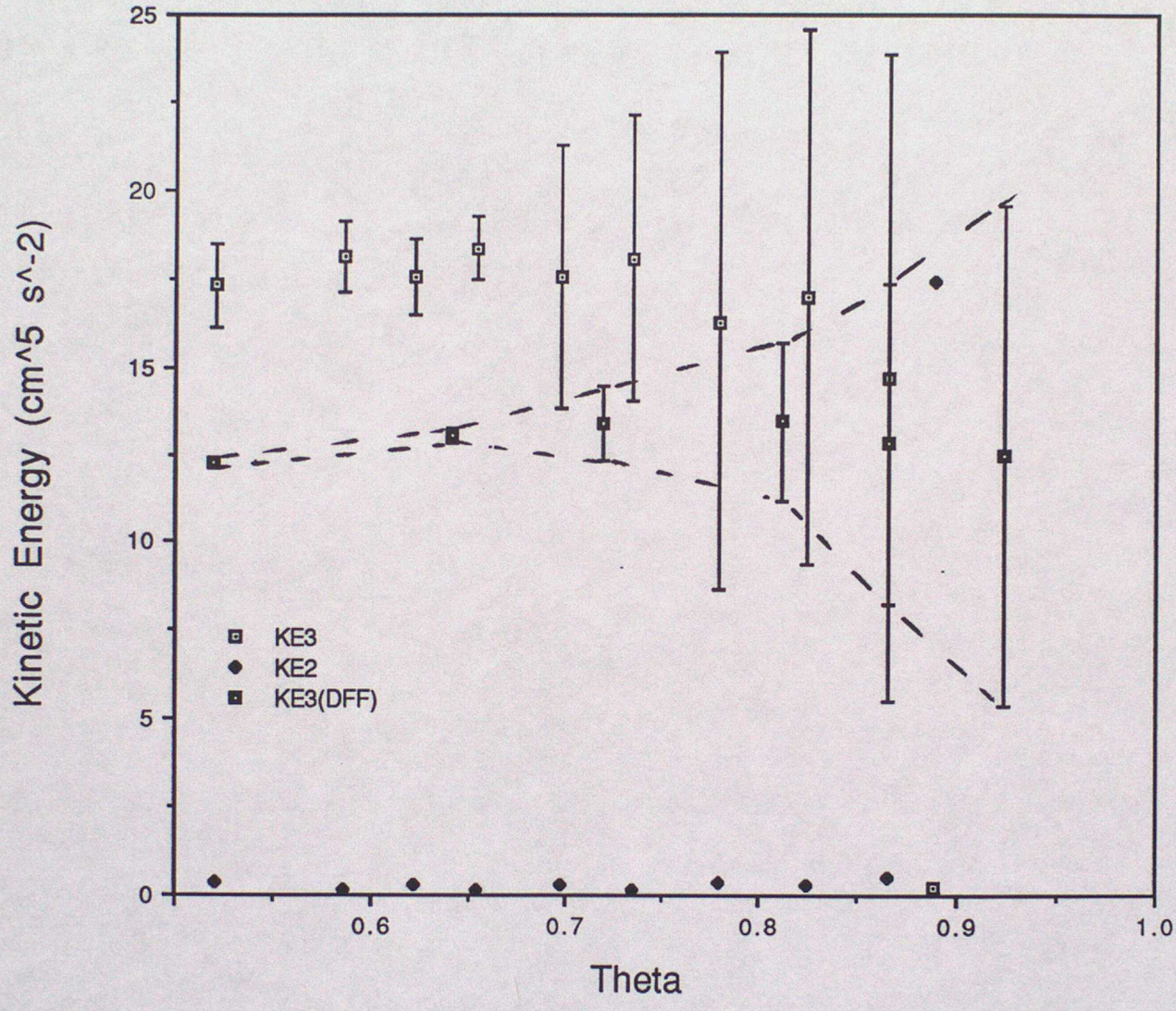
Kinetic Energy (cm^5 s^-2)
25
20
15
10
5
0
KE3
KE2
KE3(DFF)
0.6
0.7
0.8
0.9
1.0
Theta

Fig 10

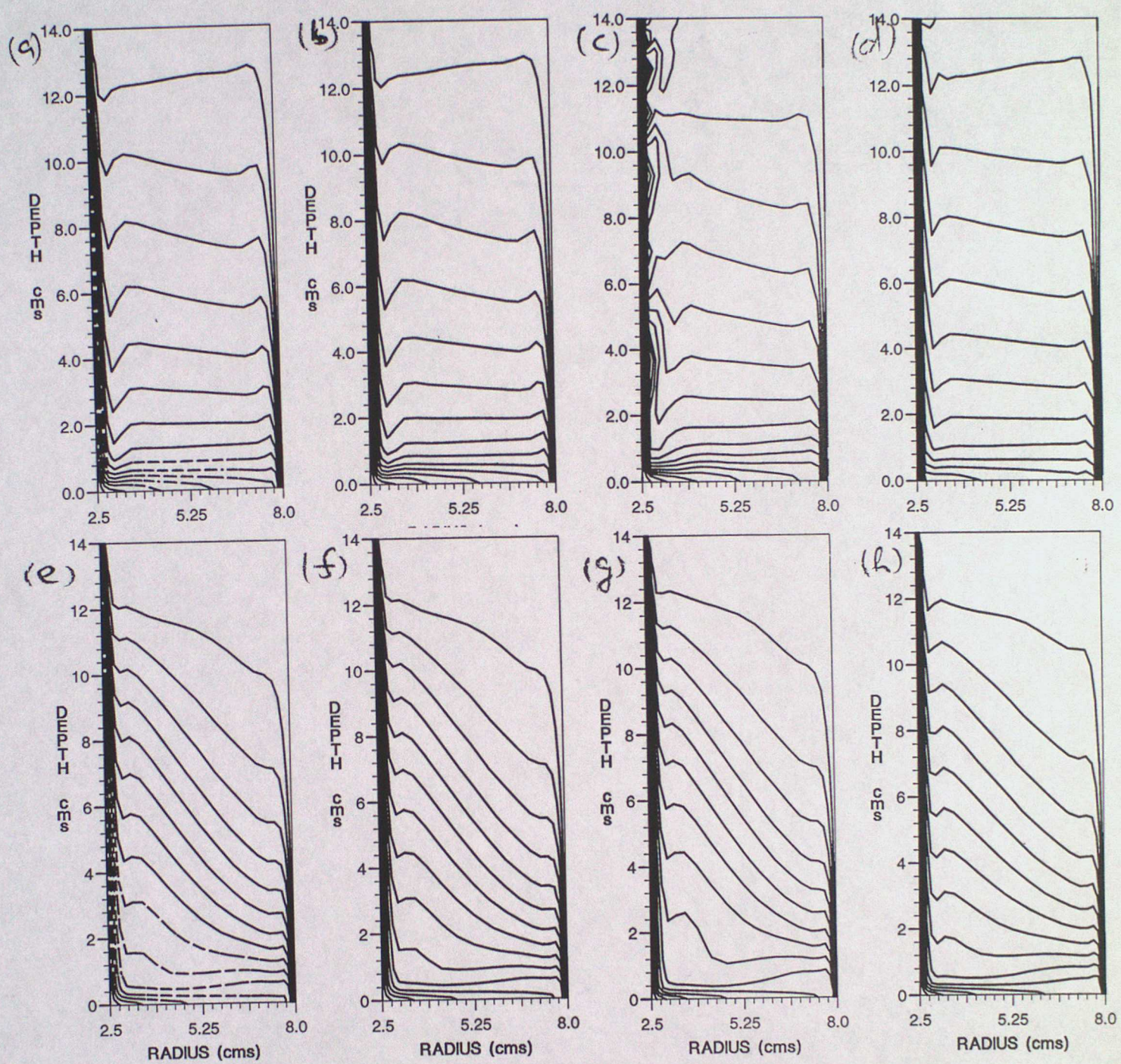
(a)
(b)
(c)
(d)
(e)
(f)
(g)
(h)
DEPTH cms
RADIUS (cms)
0.0
2.0
4.0
6.0
8.0
10.0
12.0
14.0
2.5
5.25
8.0

Fig 11

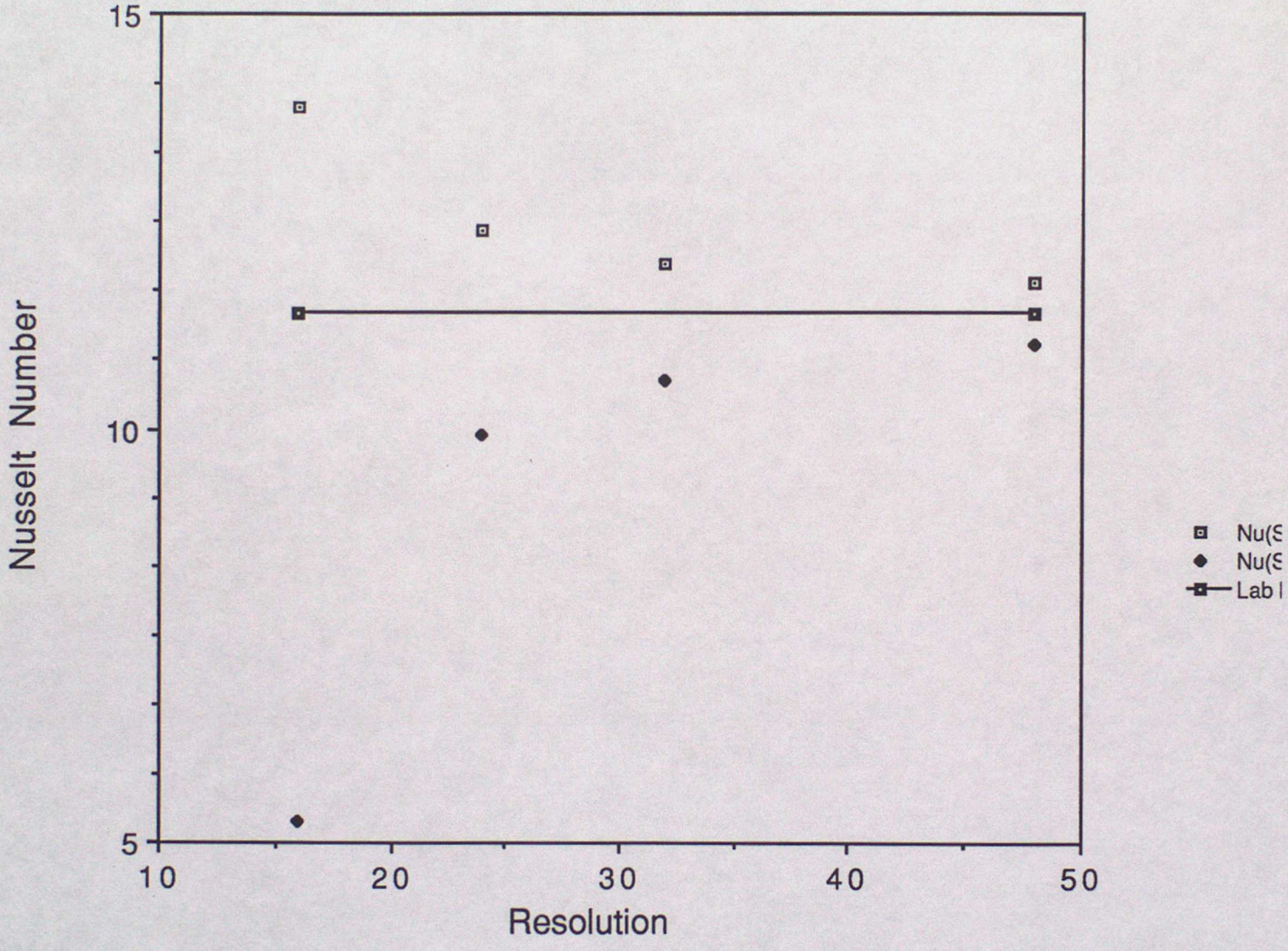

Fig 12

Data from "Steady wave spectra"

15)

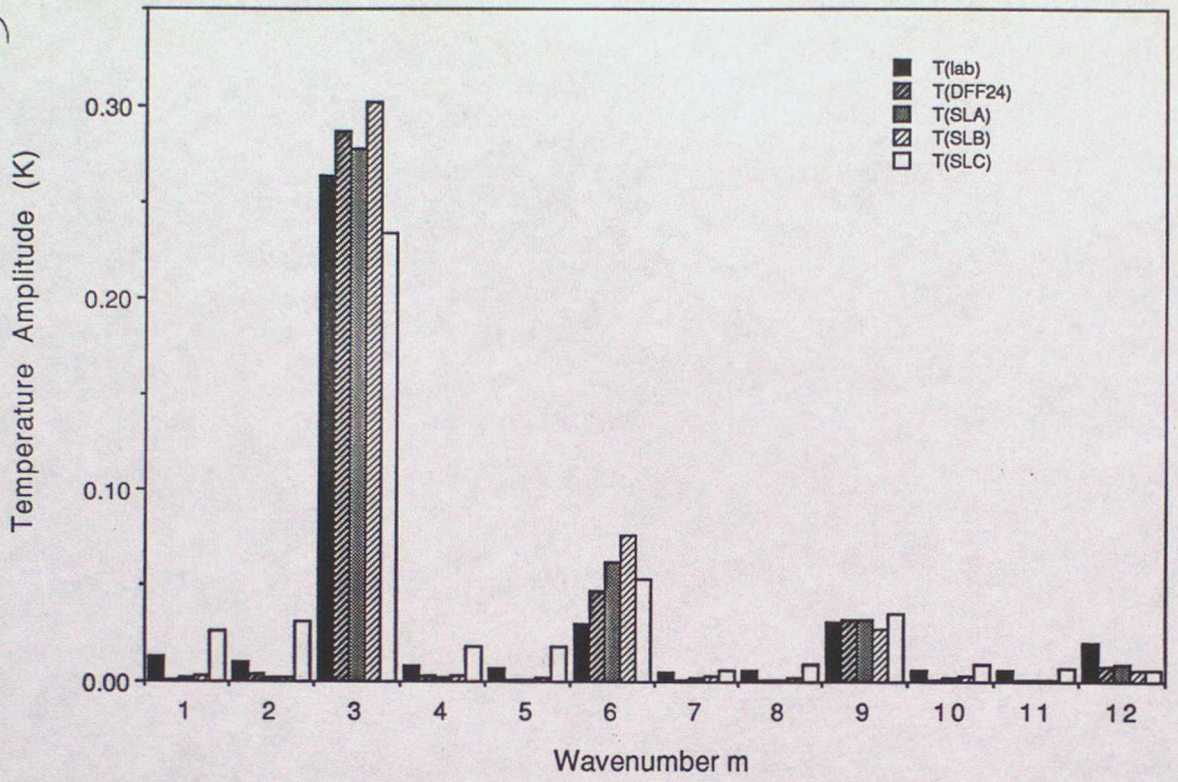

15)

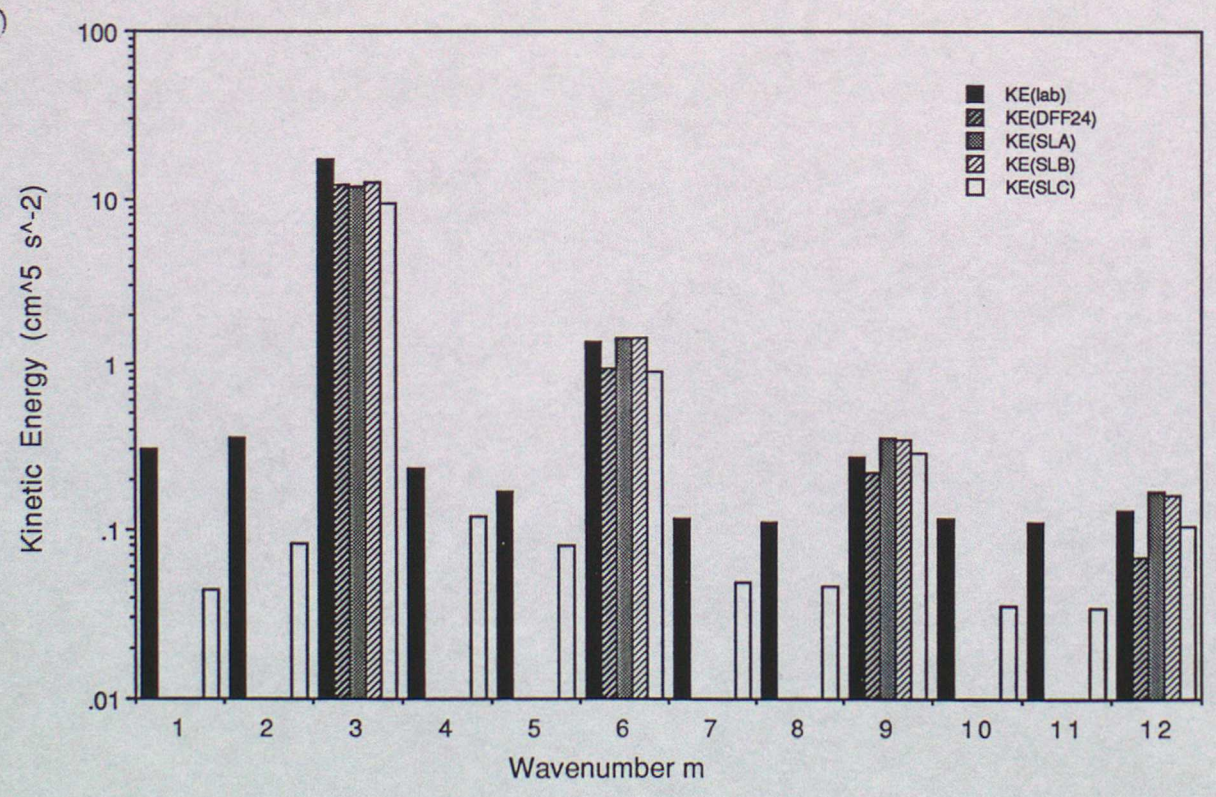

(a)

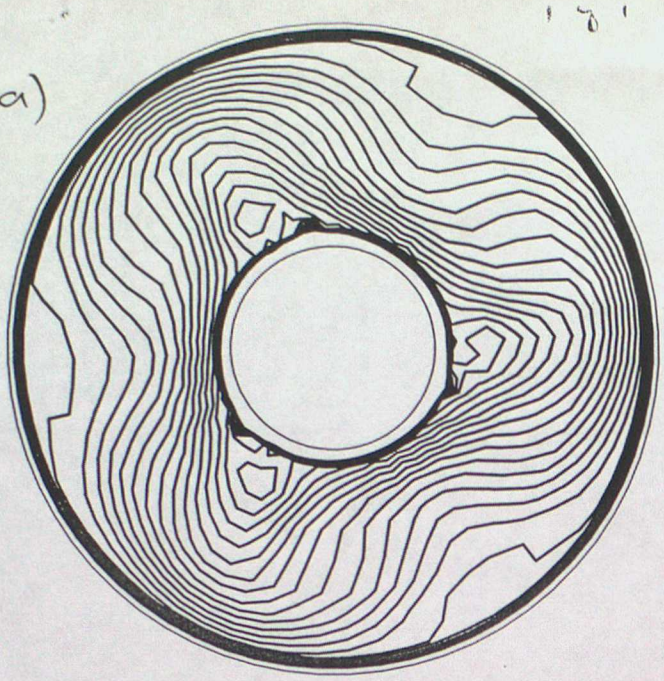

(d)

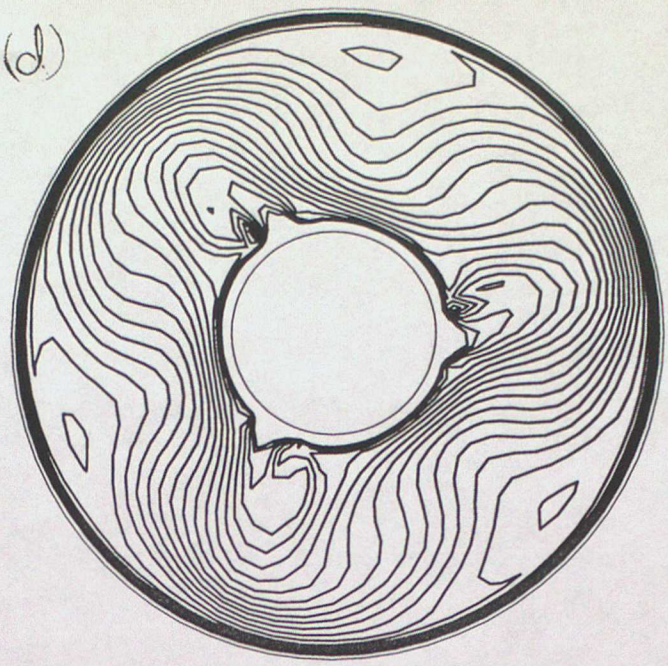

(b)

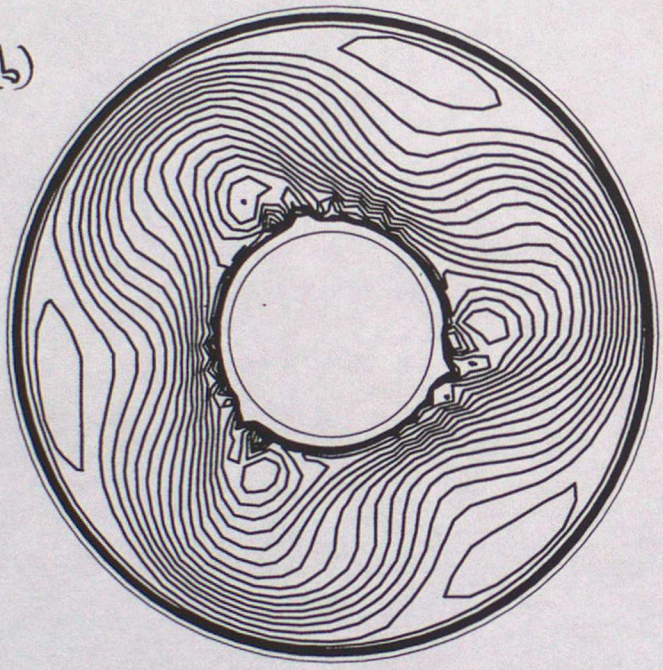

(e)

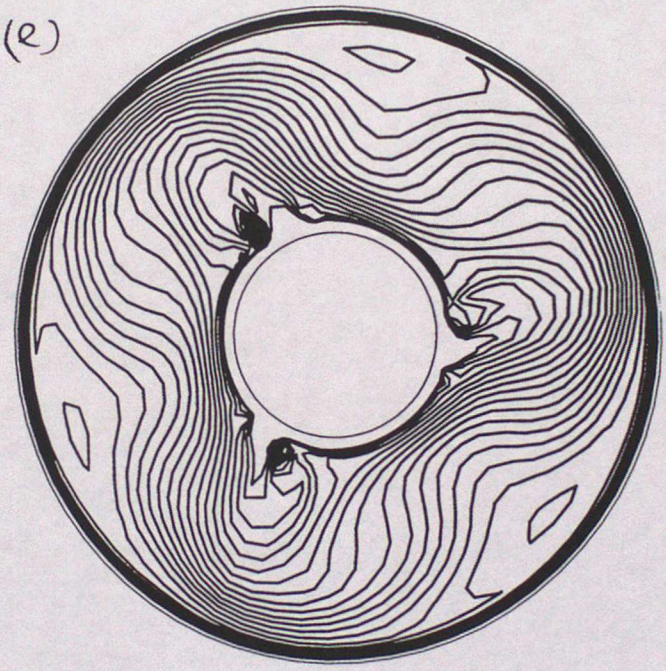

(c)

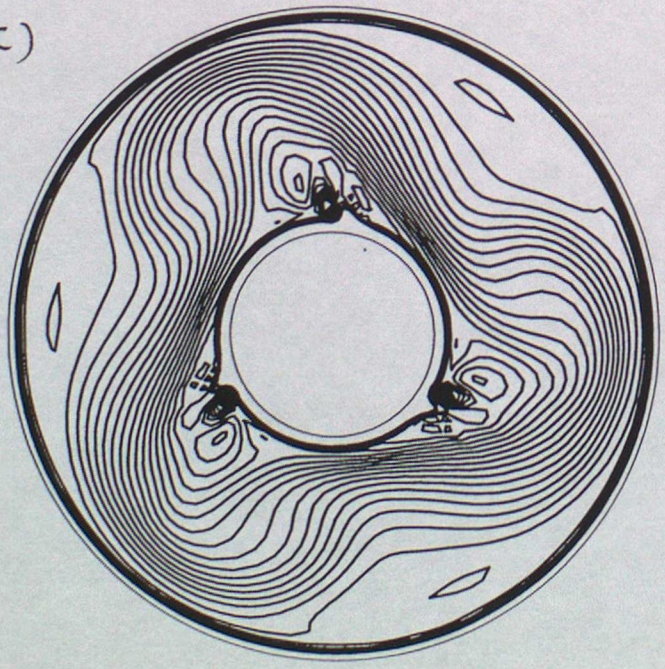

(f)

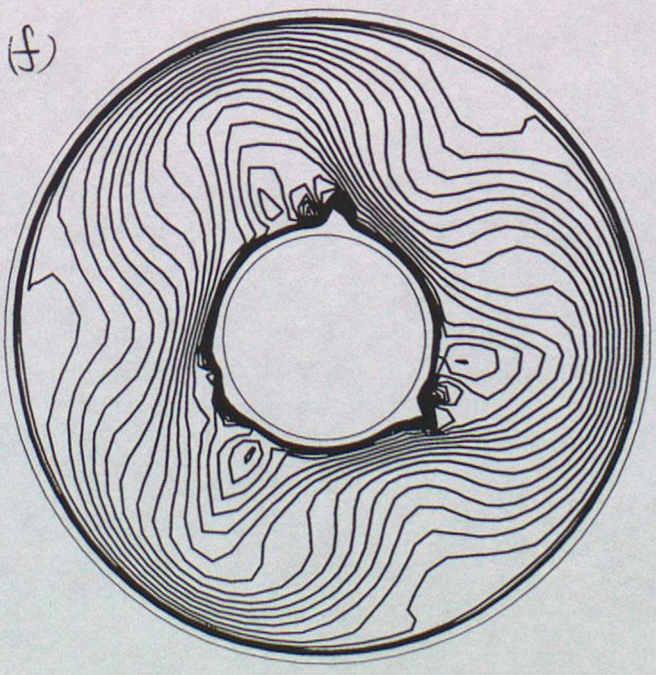

Fig. 14

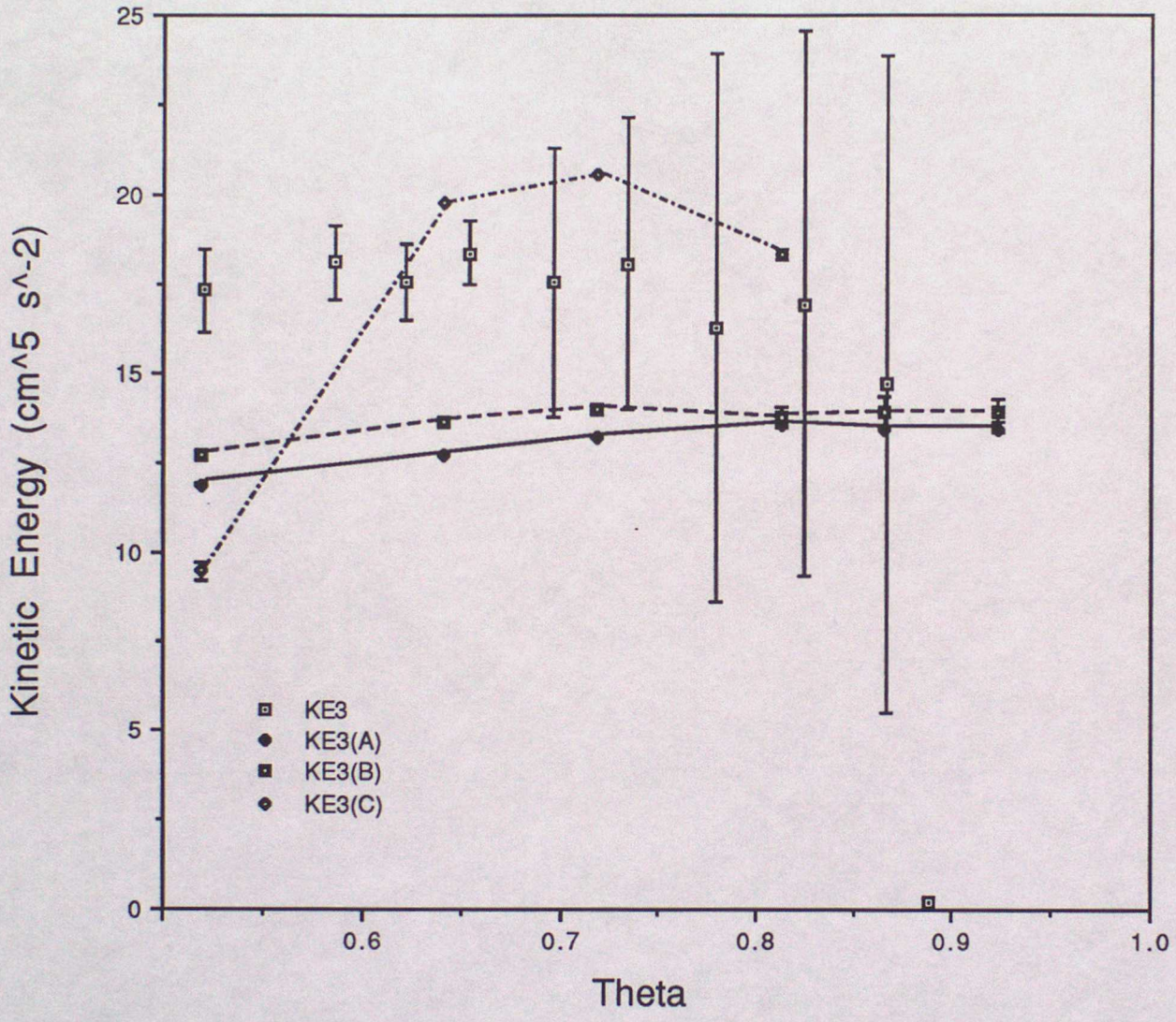
Kinetic Energy (cm^5 s^-2)
25
20
15
10
5
0
0.6
0.7
0.8
0.9
1.0
Theta
KE3
KE3(A)
KE3(B)
KE3(C)

Fig 15

(9)

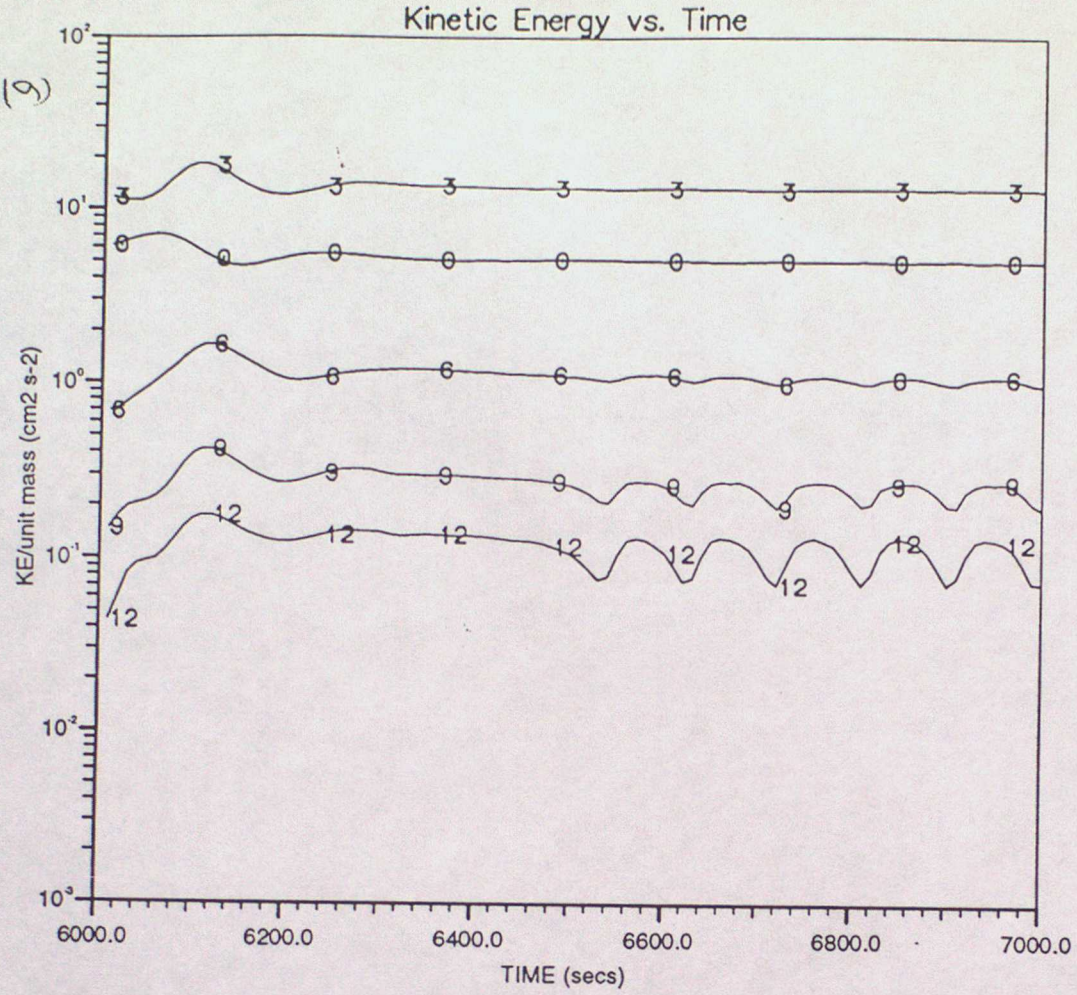
Kinetic Energy vs. Time
KE/unit mass (cm2 s-2)
TIME (secs)
6000.0
6200.0
6400.0
6600.0
6800.0
7000.0

(5)

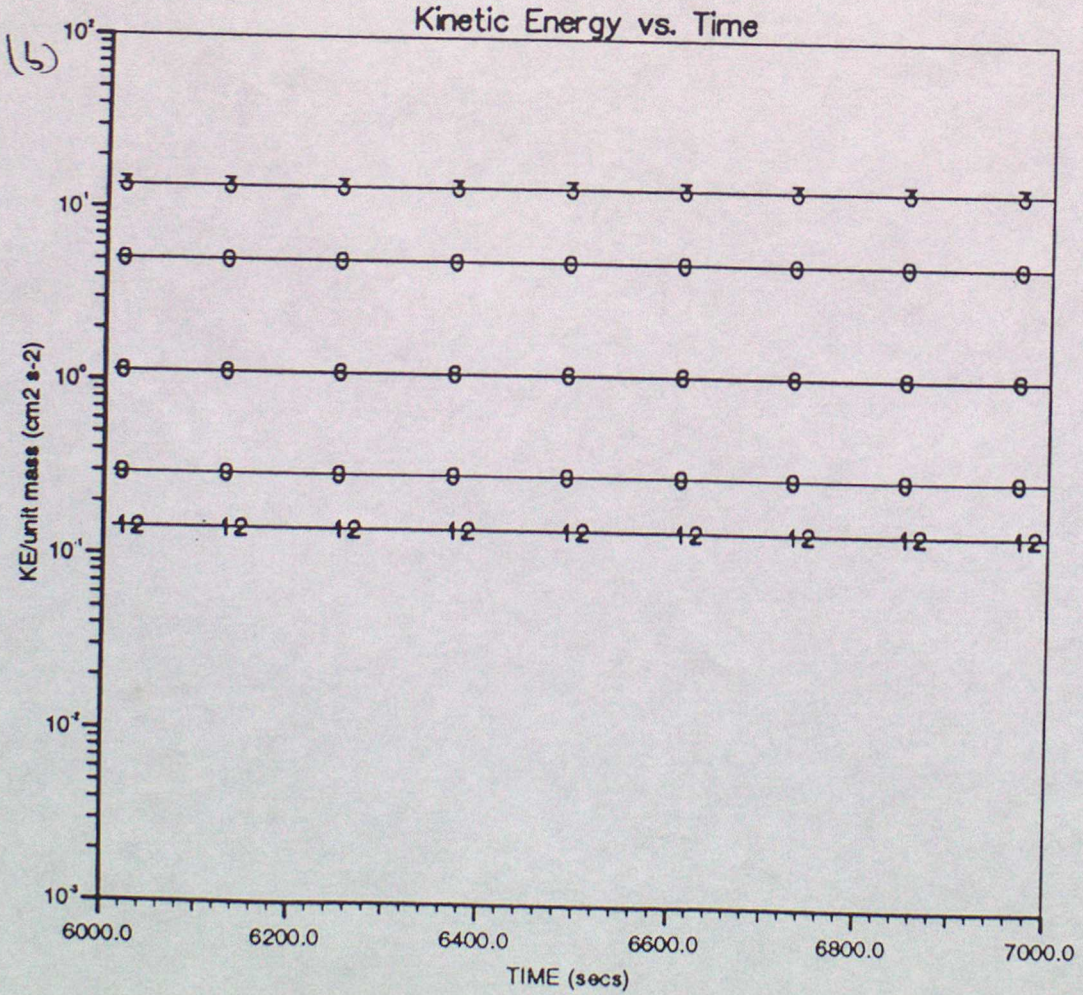
Kinetic Energy vs. Time
KE/unit mass (cm2 s-2)
TIME (secs)
6000.0
6200.0
6400.0
6600.0
6800.0
7000.0